AFRL-AFOSR-JP-TR-2020-0002

Application of Dynamical Systems Theory and Complex Systems Theory to Combustion Instability in Liquid Rocket Engines

Ri Sujith
INDIAN INSTITUTE OF TECHNOLOGY MADRAS
SARDAR PATEL ROAD
Chennai, 600036
IN

06/05/2020
Final Report

Air Force Research Laboratory
Air Force Office of Scientific Research
Asian Office of Aerospace Research and Development
Unit 45002, APO AP 96338-5002

REPORT DOCUMENTATION PAGE

Form Approved
OMB No. 0704-0188

1. REPORT DATE *(DD-MM-YYYY)*	2. REPORT TYPE	3. DATES COVERED *(From - To)*
05-06-2020	Final	07 Sep 2018 to 06 Sep 2019

4. TITLE AND SUBTITLE
Application of Dynamical Systems Theory and Complex Systems Theory to Combustion Instability in Liquid Rocket Engines

5a. CONTRACT NUMBER

5b. GRANT NUMBER
FA2386-18-1-4116

5c. PROGRAM ELEMENT NUMBER
61102F

6. AUTHOR(S)
Ri Sujith

5d. PROJECT NUMBER

5e. TASK NUMBER

5f. WORK UNIT NUMBER

7. PERFORMING ORGANIZATION NAME(S) AND ADDRESS(ES)
INDIAN INSTITUTE OF TECHNOLOGY MADRAS
SARDAR PATEL ROAD
Chennai, 600036 IN

8. PERFORMING ORGANIZATION REPORT NUMBER

9. SPONSORING/MONITORING AGENCY NAME(S) AND ADDRESS(ES)
AOARD
UNIT 45002
APO AP 96338-5002

10. SPONSOR/MONITOR'S ACRONYM(S)
AFRL/AFOSR IOA

11. SPONSOR/MONITOR'S REPORT NUMBER(S)
AFRL-AFOSR-JP-TR-2020-0002

12. DISTRIBUTION/AVAILABILITY STATEMENT
A DISTRIBUTION UNLIMITED: PB Public Release

13. SUPPLEMENTARY NOTES

14. ABSTRACT
The occurrence of thermoacoustic instabilities can potentially lead to partial or total mission failure of rockets, rising costs, increased delays, and developmental setbacks. There is a definite need to improve the definition of the onset and amplitude profile of rocket thermoacoustic instability. Analysis was done to evaluate the effect of flow, pressure, heat release rate, and the process behind self-organization which leads to the synchronization that is a major factor in thermoacoustic instability. The analysis was based on a model multi-element rocket combustor that was operated under a preheated high pressure turbulent flow rig in a fuel rich condition, to better simulate the operational conditions in a real rocket engine (or motor). The transition from small amplitude stable operation to large amplitude thermoacoustic instability occurs was highly nonlinear, consisting of typically steepened pressure wavefronts leading to the formation of shock waves. Furthermore, there was random, dynamical switching between period-3 and period-4 oscillations. To demonstrate the efficacy of measures based on dynamical systems and complex system theory, a recurrence based measure (RATIO) and two fractal based measures (multifractal spectrum width and the Hurst exponent) were established to distinguish different states of combustor operation. These measures are more robust than the existing measures such as root mean square of the oscillations, amplitude, maximum of cross correlation etc. in distinguishing the dynamical state of a rocket engine. This work successfully translated modern tools from nonlinear time series analysis to understand the complex oscillations arising in liquid rocket engines. The measures illustrated in this study can be used to validate the CFD multi-fidelity simulations used for optimizing the stability and performance metrics of the rocket comb

15. SUBJECT TERMS
nonlinear thermoacoustic instability, liquid rocket engine, dynamic systems theory

16. SECURITY CLASSIFICATION OF:			17. LIMITATION OF ABSTRACT	18. NUMBER OF PAGES	19a. NAME OF RESPONSIBLE PERSON
a. REPORT	b. ABSTRACT	c. THIS PAGE			WINDER, SHEENA
Unclassified	Unclassified	Unclassified	SAR		19b. TELEPHONE NUMBER *(Include area code)* +81-42-511-2008

APPLICATION OF DYNAMICAL SYSTEM THEORY AND COMPLEX SYSTEMS THEORY TO COMBUSTION INSTABILITY IN LIQUID ROCKET ENGINES

Final report

submitted to

Asian Office of Aerospace Research and Development

&

Air Force Research Laboratory

submitted by

R. I. Sujith, Samadhan A. Pawar, Abin Krishnan, Praveen Kasthuri and Induja Pavithran

Indian Institute of Technology Madras, Chennai 600036, India.

September 2019

This material is based upon work supported by the Air Force Office of Scientific Research under award number **FA2386-18-1-4116**.

Abstract

Liquid rockets are prone to large amplitude oscillations, commonly referred to as thermoacoustic instability. This phenomenon causes unavoidable developmental setbacks and poses a stern challenge to accomplish the mission objectives. Thermoacoustic instability arises due to the complex nonlinear interaction between the acoustic and the reactive flow subsystems in the combustion chamber. In this report, we adopt tools from dynamical systems and complex systems theory to understand the dynamical transitions from a state of stable operation to thermoacoustic instability in a self-excited model multi-element rocket combustor at Purdue University based on an oxidizer rich staged combustion cycle.

We not only study the state of thermoacoustic instability, but also, examine the dynamical transitions occurring sequentially in a range of high pressure tests. We observe that the transition to thermoacoustic instability occurs through a sequence of bursts of large amplitude periodic oscillations. Further, we show that the acoustic pressure oscillations in the combustor pertain to different dynamical states. In contrast to a simple limit cycle oscillation, we show that the system dynamics switches between period-3 and period-4 oscillations during the state of thermoacoustic instability. We show several measures based on recurrence quantification analysis and multifractal theory which can diagnose the dynamical transitions occurring in the system. We find that these measures are more robust than the existing measures in distinguishing the dynamical state of a rocket engine. Further, these measures can be used to validate models and computational fluid dynamics simulations aiming to characterize the performance and stability of rockets.

In the next part of this report, we study the slow-fast characteristics of the chamber acoustic pressure oscillations with the help of recurrence theory. We construct recurrence plots and recurrence networks to elucidate the slow-fast features of the oscillations. We also observe such features in the slow-fast oscillations of heat release rate in a model gas turbine turbulent combustor at IIT Madras. Further, we confirm these observations in three well-known models: Van der Pol model, modified Izhikevich's spiking neuron model and Hodgkin-Huxley model.

To gain a wholesome understanding of the thermoacoustic system, we need to

study the spatiotemporal behavior in addition to the temporal behavior. We utilize the high-speed CH* chemiluminescence images and hydrodynamic data generated from CFD simulations. In this chapter, we briefly describe our progress in analyzing the liquid rocket combustor using complex network and synchronization analysis.

We conclude the report with a overview of the future work continuing along these lines to help understand the problem of thermoacoustic instability in liquid rocket combustion.

Acknowledgements

This material is based upon work supported by the Air Force Office of Scientific Research under award number FA2386-18-1-4116. The authors gratefully acknowledge the funding provided by Air Force Office of Scientific Research (Grant Program Manager: Lt. Col. Sheena Winder). R. I. S. thanks Dr. Venkateswaran Sankaran (AFRL) for his numerous productive discussions. R.I.S. also thanks Dr. Ingrid Wysong (AFRL) for her interest in this work.

We are indebted to Prof. William E. Anderson, Purdue University, for colloborating with us and providing us access us to the data-sets. We thank Dr. Rohan Gejji, Purdue University, for helping us identify the correct data-sets and explaining the experimental details. Further, we thank Michael R. Orth (formerly Purdue University), for performing the experiments on the model liquid rocket combustor. We are happy to collaborate with Dr. Swanand Sardeshmukh, Purdue University, and for sharing the CFD data necessary for velocity networks.

We gratefully acknowledge the support provided by Indian Institute of Technology Madras for providing us with the necessary infrastructure and support. P. K. and I. P. thank Ms. Vedasri Godavarthi for the helpful discussions on the visualization of the recurrence network.

CONTENTS

CHAPTER 1
A BRIEF OVERVIEW ON THE NONLINEAR PHENOMENA AND COMPLEX NATURE OF LIQUID ROCKET OSCILLATIONS

Liquid rocket propulsion has become indispensable in aiding mankind for space exploration. The Apollo space program of U.S.A took a serious setback when the F-1 liquid rocket engine exhibited instabilities containing oscillations of perilous magnitudes to render the mission impossible. A special program known as Project First was established and after six more years of approximately 2000 full-scale tests, these instabilities were mitigated[1]. Similarly, these combustion instabilities have come to haunt several other space missions, notably the Soviet RD-0110 engines and the Ariane space program in Europe[2]. These instabilities came to be widely known as combustion instabilities or thermoacoustic instabilities and have been observed in liquid rocket engines, solid rocket motors, tactical and strategic missiles, aero-derivative gas turbine engines, power-producing gas turbines, industrial boilers, *etc.* Thermoacoustic instability is featured by large perilous oscillations in pressure and heat release rate arising due to the positive feedback between the acoustic pressure oscillations in a confinement and the heat release rate oscillations in the flame[3]. The occurrence of thermoacoustic instabilities can potentially lead to partial or total mission failure of rockets, rising costs, increased delays and developmental setbacks. Especially in rockets, they give rise to large amplitude thrust oscillations compromising manoeuvrability and structural integrity. As a result, thermoacoustic instability has been studied widely by academia, various national and private institutions.

Rayleigh criterion[3] was one of the earliest measures to assess the stability of combustion systems[4] . This criterion judges the balance between the acoustic driving and damping in the system. Earlier approaches based on linear stability analysis[5–9] assessed the stability of liquid rocket engines and solid rocket motors for different configurations. Crocco and Cheng[10] built the $n-\tau$ model accounting for various time lags pertaining to different processes to assess the stability of the system. This theory made a great step towards characterizing thermoacoustic instability in rocket engines of various configurations[11]. Crocco *et al.*[12] showed that the time lags of both acoustic pressure and gas velocity need to be used in the $n-\tau$ model for transverse oscillations. A similar approach was followed by Zinn *et al.*[13] to model continuous

transverse modes in three dimensions, which are more prominent in rockets. However, linear stability analysis could not conclusively explain the various dynamics observed in rocket combustors. Crocco and his co-workers have presciently predicted the importance of nonlinear dynamics[10,14,15]. Zinn and Powell[16] used the $n-\tau$ model with Galerkin method to analyze nonlinear combustion instability in liquid rocket engines. Estimates for limit cycle amplitude and triggering thresholds were obtained analytically by Mitchell *et al.*[17] for a longitudinal mode rocket motor with shock waves. We refer interested readers to an excellent recent review by Sirignano[11] for an elaborate discussion on these techniques. Apart from these brilliant analytical attempts, focus was largely skewed towards identifying the physical processes behind these combustion instabilities and attenuating these harmful oscillations with the help of baffles, Helmholtz resonators, and spray and impingement alterations[2]. Another section of research in rockets defined stability boundaries for the system for different configurations[2,9,18] and changes in the controllable operating parameters such as injector spacing inside the combustion chamber, propellant temperature, *etc.*

Rocket combustion is a highly nonlinear and dynamic process. The nonlinearities[9,18,19] may arise out of gas dynamic processes, flame interactions, boundary interactions, high thermal energy density[20] ($\mathrm{O} \sim 30\ GW/m^3$), and the turbulent base flow. Further, extreme rates of heat addition in rockets is a major source of nonlinearities in rockets. The magnitudes of the oscillations of the system variables and acoustic variables approach the order of magnitude of the mean variables. As a consequence, the nonlinearities in the system become significant and promote the transfer of energy across higher modes. The turbulent base flow induces wrinkles along the flame boundaries which are smoothed out at different rates depending on their length scales. The presence of flow separation at sharp edges, rapid flow expansions and interaction of the acoustic oscillations with the coherent structures[21,22] in the reactive flow-field add upon the nonlinearities in the system. Further, the wave steepening mechanism causes acoustic waves to turn into shockwaves[23–25]. The usage of nonlinear theory correctly predicts the saw-tooth wave profiles in pressure for cases containing shock discontinuities, while linear theory predicts smooth sinusoidal waveforms[11,23,26]. On top of all these, there exist several interactions across various subsystems such as injector hydrodynamics and flame dynamics, rendering the system complex[7,9,18,22,27,28]. Several processes occurring in rocket engines are artifacts of the nonlinearities in the system[9,25]. Limit cycle oscillations could arise due to the balance between the acoustic driving and damping

mechanisms in the system along with other limiting mechanisms like propellant flow.

A stable combustor can be excited with a finite amplitude disturbance to trigger self-sustained oscillations of considerable amplitudes. This phenomenon is known as triggering instabilities in rockets. During triggering, the system dynamics transitions to high amplitude state of oscillations through a finite amplitude perturbation above a threshold amplitude, called triggering amplitude. When the amplitude of the initial condition is less than the triggering amplitude, the system behavior decays asymptotically to a stable state. The phenomenon of triggering is observed when the system is operating in the bistable zone. In rockets, the time history of acoustic pressure oscillations is usually accompanied by a rise in the mean pressure levels. This phenomenon, known as DC shift[25] in rocket propulsion literature, exposes the rocket to dangerous amplitudes. As a result of these nonlinear behaviors, it is vital to understand the dynamics exhibited by a rocket combustor from the perspective of nonlinear dynamics.

Furthermore, much of the research focused on combustion stability assessment of rockets are based on building accurate models and computational fluid dynamics (CFD) simulations, owing to high costs involved in testing even sub-scale hardware[7,9,22,29–31]. Most of the studies have focused solely on understanding the dynamics during thermoacoustic instability. However, to characterize the various dynamics present in the system and build models that capture the relevant features, we need to characterize the dynamics during the transition from stable operation to thermoacoustic instability. Many studies exist in rocket literature[32–36] pointing out to the exponential growth of amplitudes of acoustic pressure oscillations during the transition from stable operation to unstable operation. Recently, Selvakumaran *et al.*[37] detected the signature of intermittent oscillations in heat release rate fluctuations of a composite solid propellant. Adopting tools from dynamical systems theory, Guan *et al.*[38] showed switching between period-2 and period-3 oscillations during the state of thermoacoustic instability in a full-scale solid rocket motor.

Another challenge faced by the rocket propulsion community is to identify the dynamical transitions from stable operation to thermoacoustic instability. Conventional measures[39,40] such as root mean square of the oscillations, maximum amplitude from the amplitude spectrum through Fourier transform *etc.* cannot be applied universally to all rocket combustors without apriori knowledge of the oscillation amplitudes. Different rocket combustors vary in their mean operating pressure, choice of propellants, geometry *etc.* Given the widely differ-

ent operating conditions and amplitudes observed for different rocket combustors, a measure which is bounded within a certain range of values for different rocket combustors would be a better candidate than the conventional measures to track the transition. Recently, Orth *et al.*[41] used the maximum of cross-correlation which is bounded between -1 and 1 to distinguish the stable operation from thermoacoustic instability. However, this measure cannot isolate intermittency from thermoacoustic instability. Further, it requires careful selection of the two signals to be cross-correlated. In spite of several advances, the rocket propulsion community is still in need of robust measures from dynamical systems theory to characterize and also to detect the transition from stable operation to thermoacoustic instability.

Adopting the framework of dynamical systems and complex systems, recent studies in gas turbine literature have shown immense progress towards understanding several dynamical states of combustor operation such as chaos, period-n limit cycle, and quasiperiodicity[42–44]. Several measures such as Hurst exponent[45], recurrence quantification measures[46–50], and measures from complex network analysis[51–53] have been deployed to detect the proximity to the onset of thermoacoustic instability. Further, synchronization theory has been exploited to study the coupling between the acoustic and the heat release rate oscillations[54–56]. In light of these advancements, it would be interesting to analyze the dynamics of a liquid rocket combustor using tools from complex systems and dynamical systems.

CHAPTER 2
TIME SERIES ANALYSIS OF CHAMBER ACOUSTIC PRESSURE OSCILLATIONS IN A MODEL LIQUID ROCKET COMBUSTOR DATA

In this chapter, by adopting various tools from nonlinear time series analysis, we detect the different dynamical states and also characterize the dynamical transitions observed in acoustic pressure oscillations of a liquid rocket combustor. We observe that the transition from stable operation to thermoacoustic instability occurs via intermittency, a state consisting of alternate occurrence of bursts of periodic oscillations amongst epochs of low amplitude aperiodic oscillations. Through the use of first return map, we unravel intricate features of thermoacoustic instability where the periodic dynamics alternates between period-3 and period-4 oscillations. We show that the measures based on recurrence quantification analysis and multifractal analysis can aid in detecting the dynamical transitions in the acoustic pressure oscillations, which is not possible through conventional measures.

I. METHODOLOGY OF NONLINEAR TIME SERIES ANALYSIS

In this section, we briefly describe the methodology used to perform the nonlinear time series analysis throughout the rest of the paper.

A. Phase space reconstruction

In practical applications, such as thermoacoustic instability in the combustion chamber of a rocket, it is difficult to obtain data of all the independent variables that govern the dynamics of the system. In such situations, usually only a handful of system variables (in the limiting case, at least one) are available to be acquired by an experimentalist. The dynamics of a liquid rocket combustor in the higher dimensional phase space can be reconstructed from a state variable (for example, acoustic pressure: p') by Takens' delay embedding theorem[57]. Such a reconstruction involves converting the univariate time series data into a set of delayed vectors from the appropriate choices of time delay (τ) and embedding dimension (d). We construct the vectors $x'(d) = (p'(t), p'(t+\tau), p'(t+2\tau), \ldots, p'(t+(d-1)\tau))$ from the measured pressure signal, $p'(t)$. Here, t is varied from 1 to $n-(d-1)\tau$, where n is the total number of data points in the signal. Each delay vector corresponds to a state point in the phase

space and the combination of all these vectors constitute a phase space trajectory. To perform an appropriate phase space reconstruction for a particular state of the system, we need to obtain the optimum time delay (τ) and the minimum embedding dimension (d) for the given signal. Here, τ can be estimated using average mutual information[58] or autocorrelation function[59]. The minimum embedding dimension (d) can be obtained using false nearest neighbor method[59] or alternately Cao's method[60], which we use in this study.

B. Recurrence analysis

Recurrence of state points in the phase space is a fundamental property of deterministic dynamical systems. Recurrence plots are used to visually identify the time instants at which the phase-space trajectory of the system re-visits roughly the same area in the phase space[61]. The patterns present in a recurrence plot allow us to characterize the features of the signal embedded in the d-dimensional phase space. The construction of the recurrence plot requires a prior knowledge of the optimum time delay (τ) and minimum embedding dimension (d).

The recurrence plot of any time series signal is constructed by computing the pairwise distances between the state points of the reconstructed phase space. For a time series of length n, the recurrence matrix is given by the following equation,

$$R_{ij} = \Theta(\epsilon - \left\|x'_i - x'_j\right\|) \quad i, j = 1, 2, \ldots, n - (d-1)\tau \tag{1}$$

where Θ is the Heaviside step function and ϵ is a threshold to define the neighbourhood of a state point in the reconstructed phase space. $\left\|x'_i - x'_j\right\|$ is the Euclidean distance between any two state points, i and j, on the reconstructed phase space. Whenever a state point in the phase space recurs in the predefined threshold, it is marked as a black point. Non-recurring points are marked as white points in the recurrence plot. R_{ij} is one for a black point and zero for a white point. Thus, a recurrence plot is a two-dimensional arrangement of black and white points that exhibits different patterns characterizing different dynamics of the signal.

Several statistical measures can be derived from the organization of such black and white points in the recurrence plots. Such an analysis is known as the recurrence quantification analysis of a measured signal. Measures such as determinism, recurrence rate, trapping time, entropy, laminarity, average diagonal length can be used to study the recurrence behaviour

of the phase space trajectory[62,63]. These measures could further be used to distinguish between the various dynamical states exhibited by the system. Here, we discuss the usage of determinism (DET), recurrence rate (RR), and the ratio between these quantities ($RATIO$) in the analysis of acoustic pressure data obtained experimentally from the model liquid rocket combustor.

Recurrence rate measures the density of black points in a recurrence plot and can be obtained as:

$$RR = \frac{1}{N^2} \sum_{i,j=1}^{N} R_{ij} \tag{2}$$

where $N = n - (d-1)\tau$ is the number of state vectors in the reconstructed phase space.

Determinism measures the percentage of black points in a recurrence matrix which form diagonal lines of minimum length l_{min}.

$$DET = \frac{\sum_{l=l_{min}}^{N} lP(l)}{\sum_{l=1}^{N} lP(l)} \tag{3}$$

where, $P(l)$ is the probability distribution of diagonal lines having length l and $l_{min} = 2$.

The ratio of determinism and recurrence rate ($RATIO = DET/RR$) has been introduced by Webber and Zbilut[64] to discover transitions in physiological systems.

C. Multifractal analysis

Classical Euclidean geometry deals with smooth objects which have an integer dimension. However, many things in nature contain wrinkles when observed at different levels of magnification. Such objects or signals are classified as fractals and they exhibit self-similar features at various observational scales[65]. Measures such as length, area and volume for such objects are dependent on the scale at which the measurements are performed. The logarithmic plot of the measure of the object versus the scale at which the object is measured would give a straight line with an inverse power law[65]. The absolute value of the slope of this line is known as fractal dimension (D). The framework of fractal theory can be used to describe a fractal time series which exhibits self-similarity at various timescales[66]. For a fractal time series, H quantifies the amount of correlation in the signal and is related to the fractal dimension[67] of the time series as $D = 2 - H$. If $p(t)$ is a fractal time signal whose Hurst exponent is H, then $p(ct) = p(t)/c^H$ is another fractal signal preserving the same statistics[45].

Certain complex signals cannot be described using a single fractal dimension. These signals can be described with a range of fractal dimensions and such signals are classified as multifractals. In this study, we use multifractal detrended fluctuation analysis (MFDFA)[68] to study the multifractal characteristics of the time series of acoustic pressure oscillations. To estimate the Hurst exponent, the time series ($p(t)$) is mean ($\langle p(t)\rangle$) adjusted to get a cumulative deviate series y_i as:

$$y_i = \sum_{t=1}^{i} (p(t) - \langle p(t)\rangle) \quad i = 1, 2, \ldots, n \tag{4}$$

$$\langle p(t)\rangle = \frac{\sum_{t=1}^{n} p(t)}{n}. \tag{5}$$

The deviate series is then separated into an integer number n_w non-overlapping segments of equal span w. To look for trends in the segments, a local polynomial fit ($\overline{y}_i$) is made to the deviate series y_i and the fluctuations about the trend are obtained by subtracting the polynomial fit from the deviate series. Next, a quantity known as structure function (F_w^q) of order q and span w, can then be obtained from the fluctuations for $q \neq 0$ as:

$$F_w^q = \left[\frac{1}{n_w} \sum_{i=1}^{n_w} \left(\sqrt{\frac{1}{w} \sum_{t=1}^{w} \left(y_i(t) - \overline{y}_i\right)^2} \right)^q \right]^{1/q}. \tag{6}$$

For $q = 0$, we have

$$F_w^q = \exp\left[\frac{1}{2n_w} \sum_{i=1}^{n_w} \log\left(\frac{1}{w} \sum_{t=1}^{w} \left(y_i(t) - \overline{y}_i\right)^2 \right) \right]. \tag{7}$$

The generalized Hurst exponents ($H(q)$) is then obtained from the slope[69] of the linear regime in a log-log plot of F_w^q, for a range of span sizes, w. In this study, we obtain this linear regime for 2-10 cycles[70] of the acoustic oscillations observed with a frequency of 2650 Hz during thermoacoustic instability. Thenceforth, the generalized Hurst exponents can be represented as a spectrum of singularities, $f(\alpha)$, via a Legendre transform[71].

$$\tau_q = qH^q - 1 \tag{8}$$

$$\alpha = \frac{\partial \tau_q}{\partial q} \tag{9}$$

$$f(\alpha) = q\alpha - \tau_q. \tag{10}$$

This spectrum, represented as a plot of $f(\alpha)$ against α, is known as the multifractal spectrum. The multifractal spectrum provides information on the fractal characteristics of the data. Further details regarding MFDFA can be found in the work of Kandelhart[68] and Ihlen[69].

In literature, the generalized Hurst exponent $H(q)$ for $q = 2$ is popularly known as the Hurst exponent (H). For $q = 2$, H becomes the scaling of the root mean square of the standard deviation of the fluctuations with the window size. Since its introduction, H has been used for various applications[72,73]. In thermoacoustics, Nair & Sujith[45] have used H to capture the transition from stable operation to thermoacoustic instability via intermittency in a laboratory-scale turbulent combustor. Also, Unni & Sujith[47] have used H as a precursor to detect blowout in a turbulent combustor.

II. EXPERIMENTAL SETUP

A schematic diagram of the multi-element model liquid rocket combustor is presented in Fig. 1a,b. A detailed description of the flow conditions and the experimental hardware can be found in Orth *et al.*[41] and are only briefly summarized here. The oxidizer is supplied by an oxidizer rich pre-burner that uses hydrogen as the fuel and is located upstream of an oxidizer manifold. The preburner provides oxygen with 4%-5% mass fraction of water vapor to the experiment at a mean chamber pressure of 6.55 MPa, and mean temperature of 635 K. The oxidizer manifold is sized to minimize dynamic pressure losses and provide uniform flow to each of the injection elements downstream of it. Each injector has a choke plate upstream of it to decouple any feed system dynamics from the experiment and vice versa. Methane is injected through shear coaxial injector elements at the downstream end of the oxidizer posts through a manifold with a choked inlet. The mean Mach number in the oxidizer posts is 0.25 at nominal operating conditions. A centerline-centerline injector spacing of 25.7 mm is used in the test case presented in this study. The injector exit diameter is 15.8 mm. The exit nozzle has the same aspect ratio as the combustion chamber and is designed to obtain a mean chamber pressure of approximately 1140 kPa during the test. The chamber width is chosen to drive self-excited transverse mode dynamics at a frequency of 2.65 kHz at nominal test conditions. The length of the chamber is designed for a fundamental longitudinal (1L) mode of 3475 Hz so that the transverse mode harmonic frequency does not coincide with

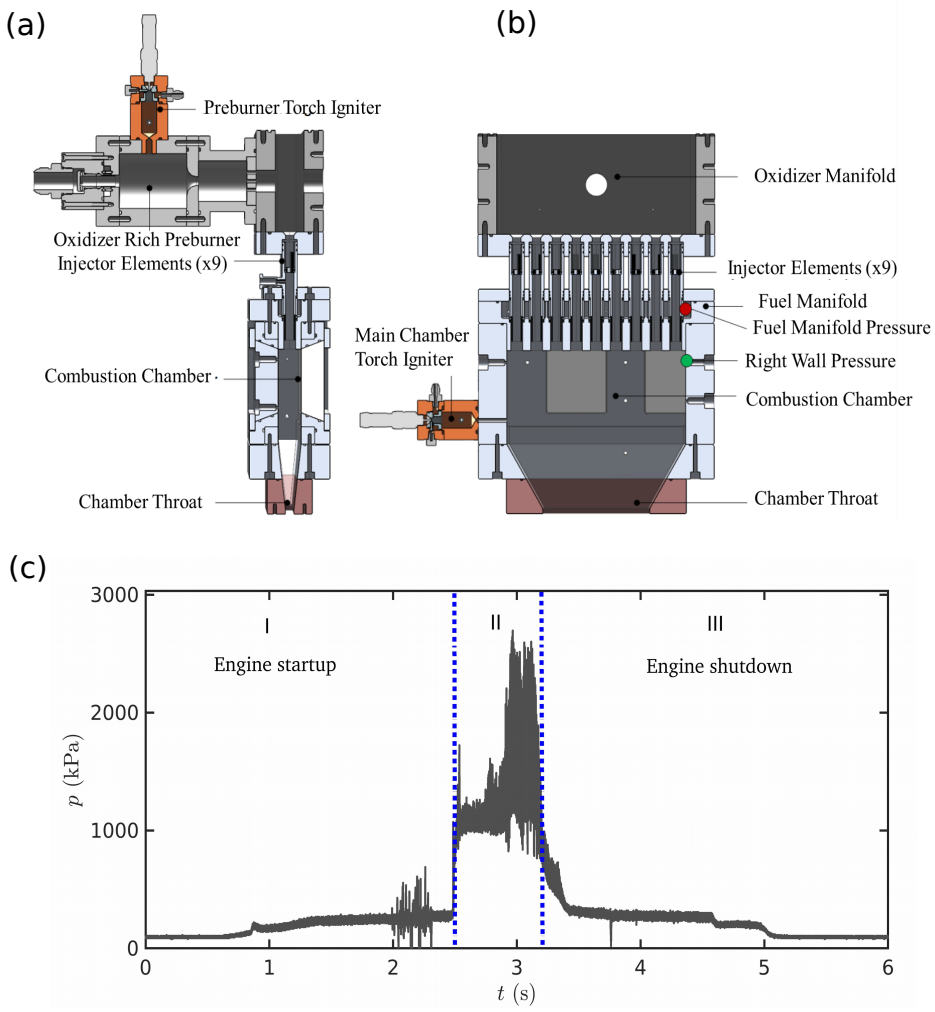

FIG. 1. (a) The side view of the experimental setup used to excite transverse instabilities in the laboratory scale multi-element liquid rocket combustor. (b) A detailed view of the main combustor is shown. The entire experiment lasts for 6 seconds. (c) A representative time series of acoustic pressure oscillations obtained from the pressure transducer located at right side wall of the combustor during Test - C. The dashed lines demarcate the test time interval (i.e. region-II) from the engine startup and shutdown durations.

the 1L mode or its harmonics.

The combustion chamber is instrumented densely with high frequency pressure transducers and K-Type thermocouples. Piezoresistive Kulite WCT-312M sensors sampled at 250 kHz are used to measure the pressure in the propellant manifolds, oxidizer post, and the

combustion chamber. The sensors are mounted in a recess cavity to avoid thermal saturation effects. The cavity is designed as a Helmholtz resonator with a resonance frequency of 22.4 kHz. The location of the pressure transducers used for the analysis are labeled in Fig. 1b.

A representative time series of acoustic pressure oscillations obtained from the pressure transducer located at the right side wall of the combustor is shown in Fig. 1c. The time interval in region I corresponds to starting of the preburner and the ignition of the main chamber. The first jump in the pressure signal close to 1 s corresponds to the start of the preburner and the second jump at 2.5 s corresponds to the ignition of the main chamber. Region III pertains to the shutdown of the engine. The acoustic pressure oscillations in region II are of prime interest in this study, as this interval of the signal represents the actual dynamical transitions from stable operation to thermoacoustic instability in the liquid rocket combustor.

III. RESULTS AND DISCUSSIONS

In this section, we characterize the temporal behavior of acoustic pressure oscillations observed during the onset of thermoacoustic instability in the liquid rocket combustor. Towards this purpose, we examine the time series of the chamber acoustic pressure oscillations, as shown in Fig. 2, acquired for the same operating conditions (working fluids, flow rates, upstream pressures and temperatures) and the injector configurations. However, we notice that although the operating conditions are the same during experiments, the dynamics arising out of the combustor is different during each trial. The data-sets chosen for the analysis along with the dynamical transitions observed are summarized in Table. I.

A. Classification of dynamical states

For Test - A (Fig. 2a), we observe that the time series is entirely composed of stable operation, exhibiting low amplitude aperiodic oscillations. For Test - B (Fig. 2b), we observe small epochs of marginally large amplitude periodic oscillations interspersed within the aperiodic oscillations of the signal. We refer to this dynamical state as intermittency. In general, intermittency refers to a dynamical state composed of high amplitude bursts of periodic oscillations amidst epochs of low amplitude aperiodic oscillations in an apparently

Data-set	Dynamical transitions observed
Test - A	Stable operation
Test - B	Intermittency
Test - C	Stable operation ⇒ Intermittency ⇒ Thermoacoustic instability
Test - D	Intermittency ⇒ Thermoacoustic instability
Test - E	Intermittency ⇒ Thermoacoustic instability

TABLE I. The list of data-sets chosen for analysis and the corresponding dynamical transitions observed in each test.

random manner[46]. Next, we obtain a transition from stable operation to thermoacoustic instability via intermittency for Test - C (Fig. 2c). Here, thermoacoustic instability is comprised of large amplitude periodic oscillations. For Test - D (Fig. 2d) and Test - E (Fig. 2e), we detect only two dynamical states: intermittency followed by thermoacoustic instability without the occurrence of a stable combustor operation. However, the time spent in the periodic epoch of intermittency is higher during Test - E than that for Test - D. The reasons behind such a difference in the dynamics of the combustor behaviour for the same operating conditions remain unanswered.

A careful observation of the dynamics of the liquid rocket combustor shows the existence of three primary dynamical states in the acoustic pressure oscillations. These states are stable operation (low amplitude aperiodicity), intermittency (epochs of periodicity interspersed between epochs of aperiodicity in an apparently random manner), and thermoacoustic instability (epochs of sustained periodicity). During the periodic epochs of intermittency and thermoacoustic instability, we observe that the periodic waveform nearly takes the shape of a saw tooth wave profile. Further, we notice that the state of intermittency always precedes the onset of thermoacoustic instability. Such an observation is different from previous descriptions of the onset of thermoacoustic instability where the transition from small amplitudes to large amplitudes is reported through an exponential growth[32–36]. Recently, Orth *et al.*[41] band-pass filtered the time series of acoustic pressure oscillations in the same model multi-element combustor, used in the present study. When the frequencies pertaining to the fundamental mode are band-passed, they observed the presence of an exponential growth rate in the amplitude of oscillations. They also observed a similar exponential growth rate

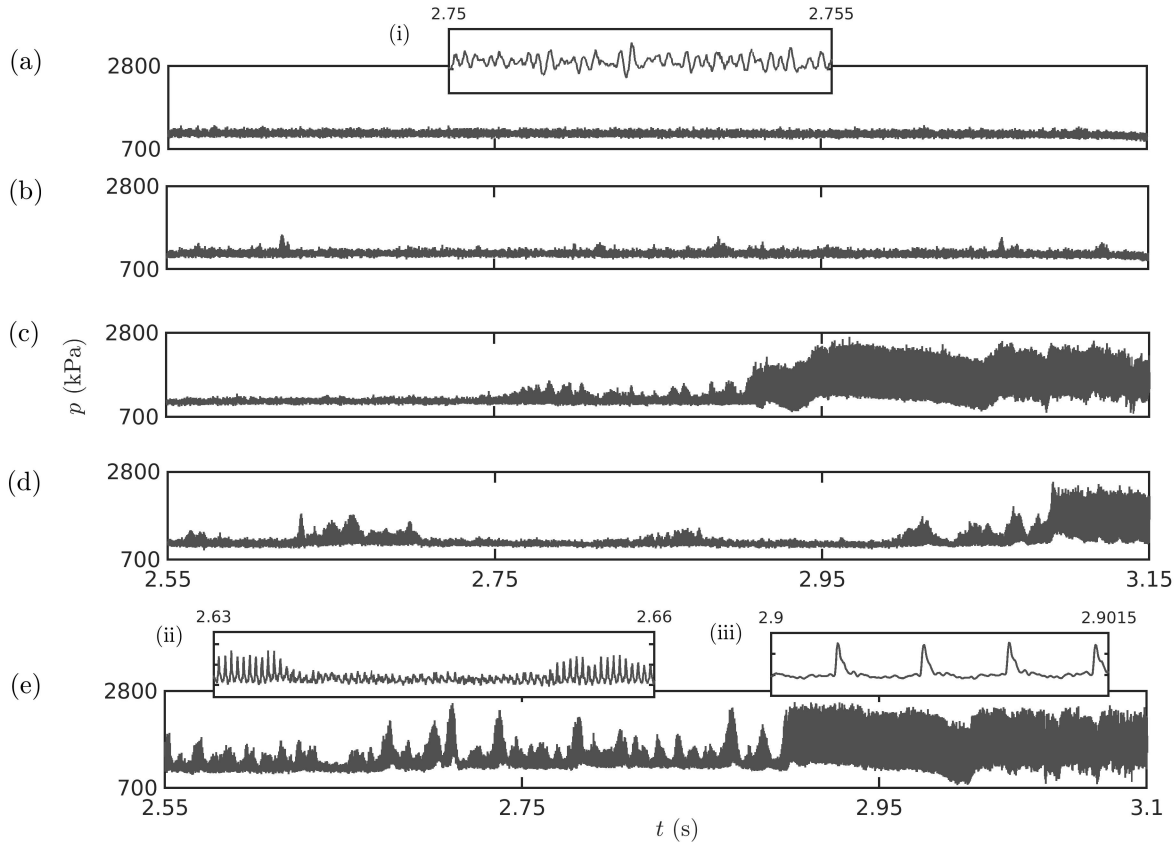

FIG. 2. Time series of acoustic pressure fluctuations acquired at the right side wall of the combustion chamber in the interval of interest marked II in Fig. 1c for tests: (a) Test - A (stable operation), (b) Test - B (intermittency), (c) Test - C (stable operation - intermittency - thermoacoustic instability), (d) Test - D (intermittency - thermoacoustic instability), and (e) Test - E (intermittency - thermoacoustic instability). The representative portions of the various dynamical states are zoomed and shown in the insets: (i) stable operation, (ii) intermittency and (iii) thermoacoustic instability.

when the harmonic frequencies are band-passed. However, in the present study, we analyze the time series with its entire frequency content preserved. In this study, we characterize the dynamical features of the representative portions of the time series pertaining to these three dynamical states observed during different trials of experiments. We choose stable operation of Test - A, intermittency from Test - E, and thermoacoustic instability from Test - E. Next, we will look into the frequency content present in these three dynamical states.

The amplitude spectrum with a frequency resolution of 12 Hz generated out of the fast Fourier Transform (FFT) algorithm is plotted in Fig. 3. For stable operation (Fig. 3a),

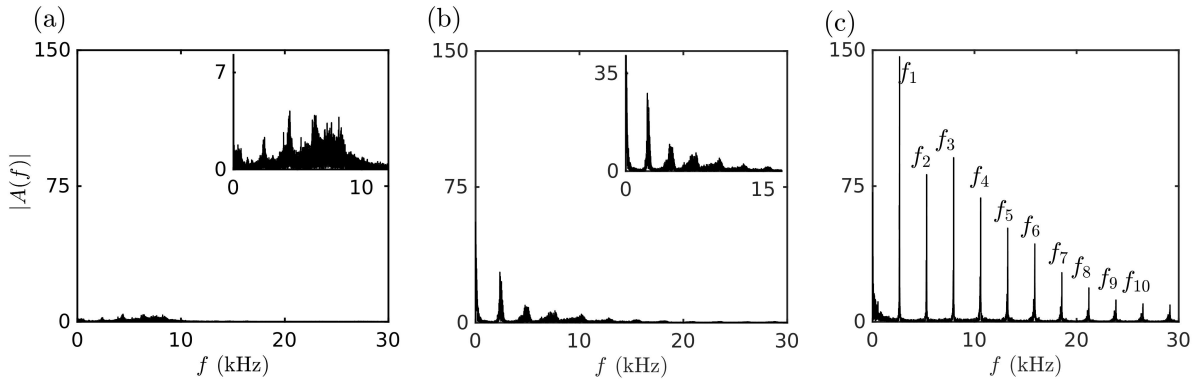

FIG. 3. The amplitude spectrum obtained through fast Fourier transform (FFT) with a frequency resolution of 12 Hz for (a) stable state of Test - A, (b) intermittency in Test - E, and (c) thermoacoustic instability in Test - E. The zoomed insets are shown for (a) stable operation and (b) intermittency.

we observe that the amplitude spectrum is broadband containing a wide range of frequencies. During intermittency (Fig. 3b), we observe a dominant peak emerging around 2500 Hz amidst the neighbouring band of frequencies. During thermoacoustic instability (Fig. 3c), we obtain a sharp peak at $f_1 = 2650$ Hz along with several of its harmonics (nf_1) of considerable amplitudes. We have marked only the first ten harmonics ($f_2 = 2f_1$ to $f_{10} = 10f_1$) for conciseness. The presence of several harmonics of considerable amplitudes during thermoacoustic instability is due to the spiky nature of the signal caused by the steepening of the compression wave front into a shock wave[25,26]. The shift in the dominant frequency in time is attributed to the increase in mean temperature during the transition.

B. Phase space reconstruction

To probe the hidden features of the dynamics during each state, we reconstruct the phase space traced by the acoustic pressure oscillations. For this purpose, we need to evaluate the optimum time delay and minimum embedding dimension for each state. Further, to estimate the optimum time delay, we plot the average mutual information (AMI) for different time lags[58] as shown in the first column of Fig. 4. AMI measures the mutual dependence of the signal and its delayed version at two different time instants. The first minima of the AMI can be used as the optimum time delay for the construction of the phase space. However,

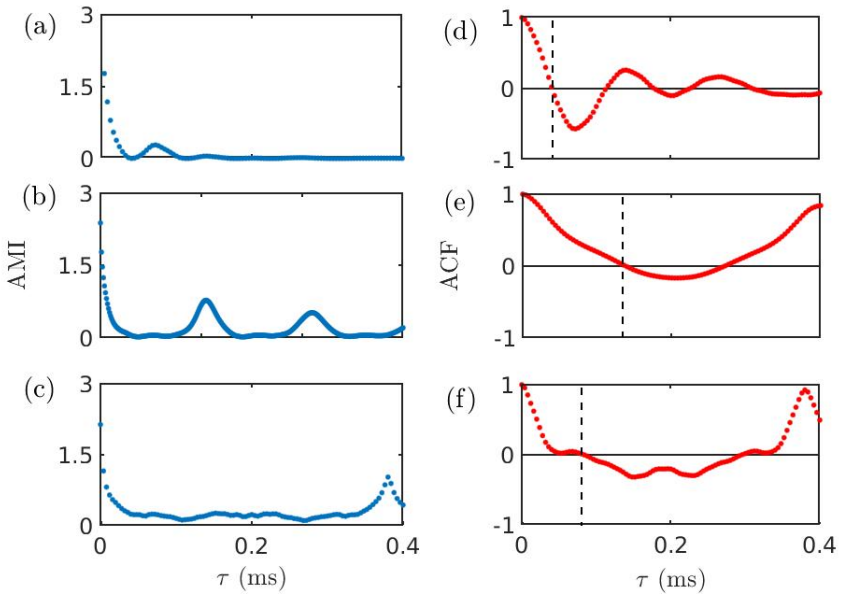

FIG. 4. (a-c) Average mutual information (AMI) and (d-f) autocorrelation function (ACF) are evaluated to estimate the optimum time delay required for the construction of phase portrait during (a, d) stable operation of Test - A, (b, e) intermittency in Test - E, and (c, f) thermoacoustic instability of Test - E.

we observe that the optimum time delay cannot be unambiguously determined using AMI (Fig. 4a-c), due to the difficulty in clearly identifying the first local minima, especially in Fig. 4b,c. Hence, we turn to the autocorrelation function (ACF) to estimate the optimum time delays[59].

Autocorrelation function (ACF) calculates the linear correlation between a time series and its delayed copy of the same time series. The value of ACF ranges between -1 to 1. The optimum time delays obtained from ACF corresponds to the first zero crossing in the plot, which are denoted by dashed lines in (Fig. 4d-f). The corresponding optimum time delays for stable operation, intermittency, and thermoacoustic instability are 0.04 ms, 0.136 ms and 0.084 ms, respectively.

Further, we need to estimate the minimum embedding dimension required for the phase space reconstruction. We rely on Cao's method[60] to identify the minimum embedding dimension. The two parameters: $E1$ and $E2$ are evaluated for a range of embedding dimensions from 1 to 20. $E1$ measures the ratio of mean distances between two points in the phase space in two successive embedding dimensions. When the sufficient embedding dimension

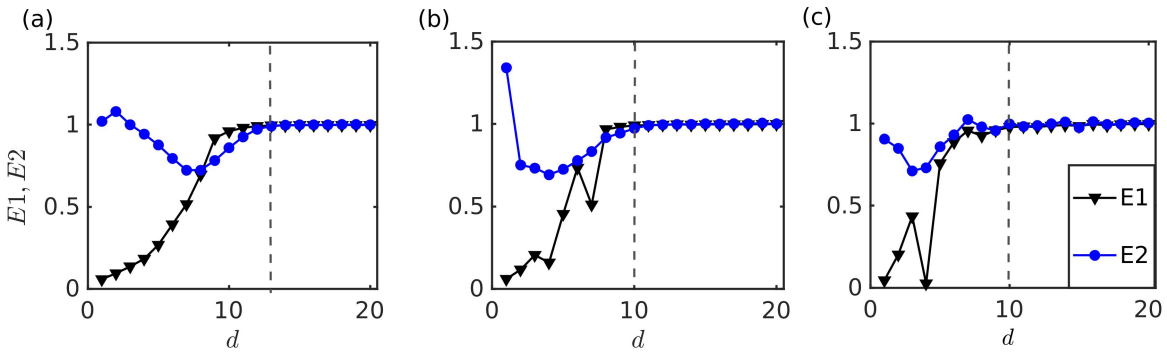

FIG. 5. (a-c) The optimum embedding dimension required for phase space reconstruction is obtained by Cao's method, evaluating quantities, $E1$ (black) and $E2$ (blue), during (a) stable operation of Test - A, (b)intermittency in Test - E, and (c) thermoacoustic instability for Test - E, respectively. The optimum embedding dimension are denoted by dashed lines.

is attained, $E1$ attains a value close to 1 and remains constant for further increments in embedding dimension. $E2$ is a quantity which can distinguish between deterministic and stochastic signals. For a completely random signal, $E2$ remains nearly unity for any embedding dimension[60]. For deterministic signals, $E2$ varies for lower embedding dimensions and saturates beyond a certain embedding dimension.

The optimum embedding dimension is the dimension, denoted by dashed lines in Fig. 5a-c, for which $E1$ and $E2$ starts to become invariant with further increase in dimension (d). In addition, we observe that $E2$ is not unity for some embedding dimensions, denoting that the dynamics during stable operation are not completely stochastic. The minimum embedding dimension chosen is 13 for stable operation (Fig. 5a), and 10 for both intermittency (Fig. 5b) and thermoacoustic instability (Fig. 5c).

With the optimum time delays obtained for each state, we plot the three-dimensional phase portraits for stable operation, intermittency, and thermoacoustic instability in Fig. 6a-c. We observe that the phase portraits during stable operation in Fig. 6a is cluttered and has no distinct repeating pattern corresponding to the low amplitude aperiodic oscillations. However, during thermoacoustic instability in Fig. 6c, we obtain a pattern (marked 1-7 in order) which repeats at equal intervals of time. The phase portrait of this state shows a stretched trefoil-knot like structure, similar to that observed in gas phase detonations[74]. This structure is radically different from the phase portrait of thermoacoustic instability observed for gas turbine combustors, which mostly trace out a ring or elliptical orbit[42,54].

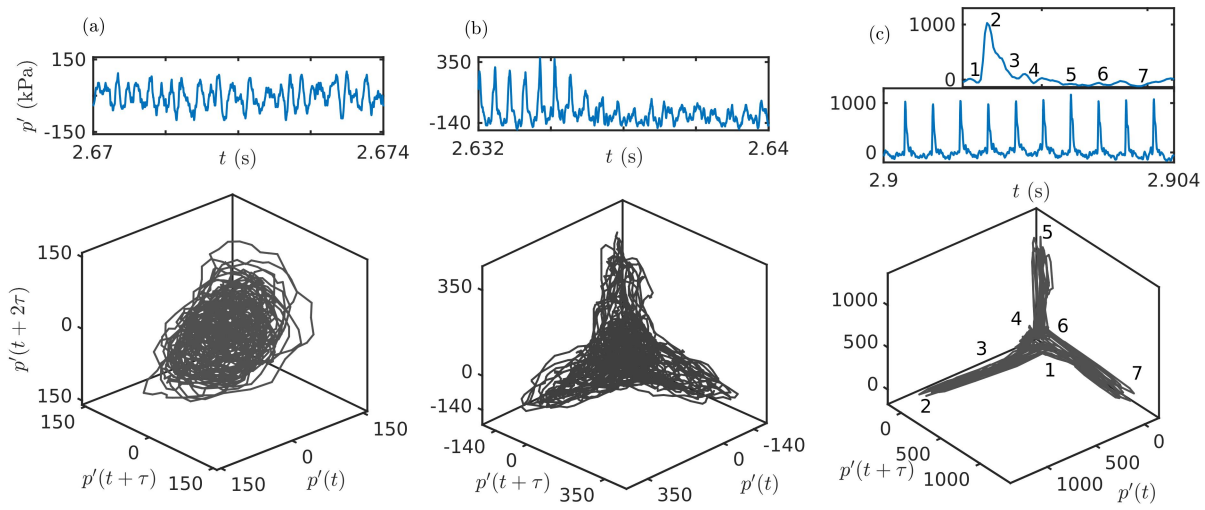

FIG. 6. The phase portraits visualized using the estimated optimum time delays and embedding dimensions in Fig. 4 & 5 for (a) stable state of Test - A, (b) intermittency in Test - E, and (c) thermoacoustic instability in Test - E. The phase portraits are reconstructed using the corresponding time interval depicted for each dynamical state. The trajectory traced out by the phase portrait for one cycle of oscillation during thermoacoustic instability is marked 1-7 in the corresponding waveform shown in the inset.

During thermoacoustic instability in this rocket combustor, due to an increase in the speed of sound because of rising temperature and convective effects in the compression phase, the waveform tends to catch up with the expansion front[23,24]. This leads to the steepening of the compression wave front into a shock wave. As a result, the pressure wave front has a faster growth in the amplitude during the compression phase compared to the slow decay of the oscillation in the expansion phase. This characteristic behavior is captured faithfully in the corresponding phase portrait wherein the phase space trajectory spends relatively shorter times during the compression phase (points 1-2 in Fig. 6c) compared to the expansion phase (points 2-7 in Fig. 6c) of the signal. During intermittency in Fig. 6b, we obtain a phase portrait bearing some resemblance to the phase portrait during thermoacoustic instability. The presence of amplitude modulation during periodic oscillations and the aperiodic oscillations corrugates the phase portrait of intermittency.

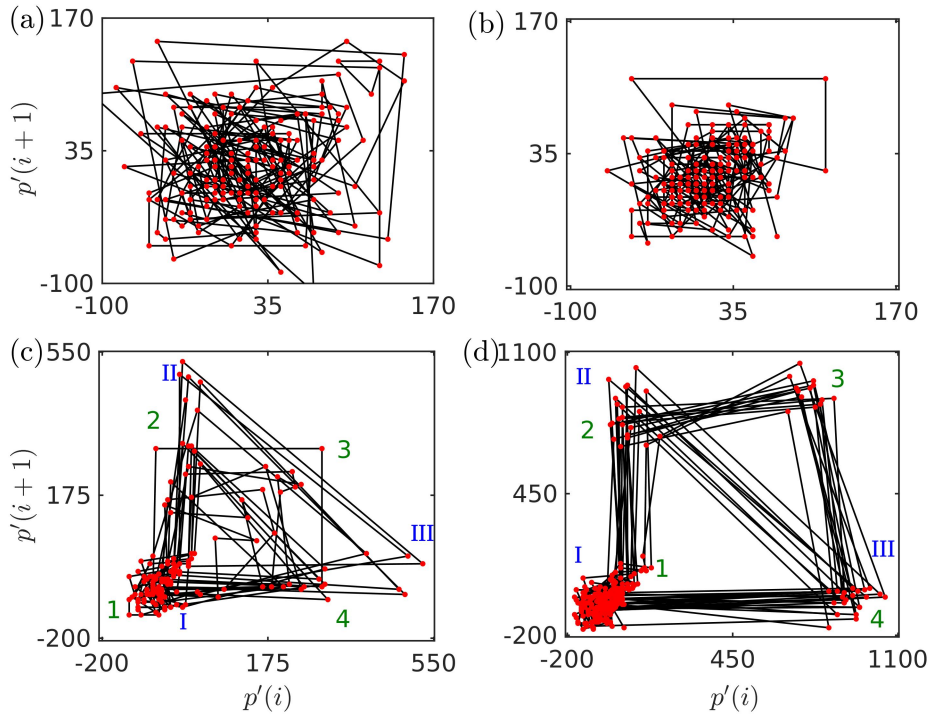

FIG. 7. Poincare sections or first return maps of the acoustic pressure oscillations during (a) stable operation in Test - A, (b) aperiodic portion of intermittency in Test - D, (c) periodic portion of intermittency in Test - E, and (d) thermoacoustic instability of Test - E.

C. Return maps

A Poincare map or first return map preserves many properties of periodic, quasi-periodic and chaotic orbits[59]. Hence, we use a return map, tracking the successive local maxima of the signal, to probe the dynamics. In Fig. 7, the first return map tracking the local maxima of the acoustic pressure oscillations during stable operation, intermittency: aperiodic and periodic epochs, and thermoacoustic instability are plotted.

The trajectory traced by the return map helps us in identifying the precise dynamical state which is sometimes not apparent from the visual inspection of the three dimensional phase portrait. In a first return map, a point is observed for limit cycle oscillations with period-1, a ring is observed for the quasiperiodic oscillations, and a clutter of points for a chaotic signal[75]. Also, if the consecutive dots traced in the return map of period-n oscillations are joined, it results in the trajectory of a n-sided polygon.

The aperiodic oscillations (see Fig. 7a,b) during stable operation and intermittency show

a clutter of trajectories without exhibiting any specific pattern. However, for periodic oscillations (Fig. 7c,d) during both intermittency and thermoacoustic instability, we observe the random occurrence of period-3 and period-4 oscillations as shown by triangles (I-II-III) and quadrilaterals (1-2-3-4), respectively, in their first return maps. This further suggests that the state of thermoacoustic instability is non-trivial and is not the same as the period-1 limit cycle oscillations which is usually observed for gas turbine engines. It is particularly interesting to note that a similar switching between period-2 and period-3 limit cycle dynamics have been reported recently for a full-scale solid rocket motor[38]. At this juncture, we must note that caution must be exercised while applying tools designed to detect conventional period-1 limit cycle oscillations as they might fail for such complex period-3 and period-4 oscillations.

D. Recurrence plots

The phase portraits of high-dimensional attractors are usually visualized by projecting them into the lower dimensions. However, a lot of information will be lost when the phase space is condensed into lower dimenisons. Eckmann *et al.*[61] proposed a visual representation tool, known as recurrence plot that enables us to investigate the behavior of n-dimensional phase space trajectory through a two-dimensional representation of its recurrences. The recurrence plot contains unique patterns for each kind of oscillation. For example, periodic oscillations are represented by continuous diagonal lines, because the trajectory of such signals revisits roughly the same region of phase space in equal intervals of time. For random signals, we obtain a grainy structure in the recurrence plot. For chaotic signals, unlike random signal, one would obtain isolated short lines parallel to the main diagonal line[76]. For a detailed description on recurrence plots, we encourage the reader to see Marwan *et al.*[77].

Recurrence plots (RP) for the acoustic pressure oscillations during the stable operation, intermittency (both aperiodic and periodic epochs), and thermoacoustic instability are shown in Fig. 8. The black patches during the occurrence of aperiodic oscillations in Fig. 8a,b correspond to the trajectory trapped within a small region in the phase space. The short (or broken) lengths of diagonal lines in RP (see zoomed inset in Fig. 8a,b) during both stable operation and aperiodic region of intermittency imply deterministic behavior,

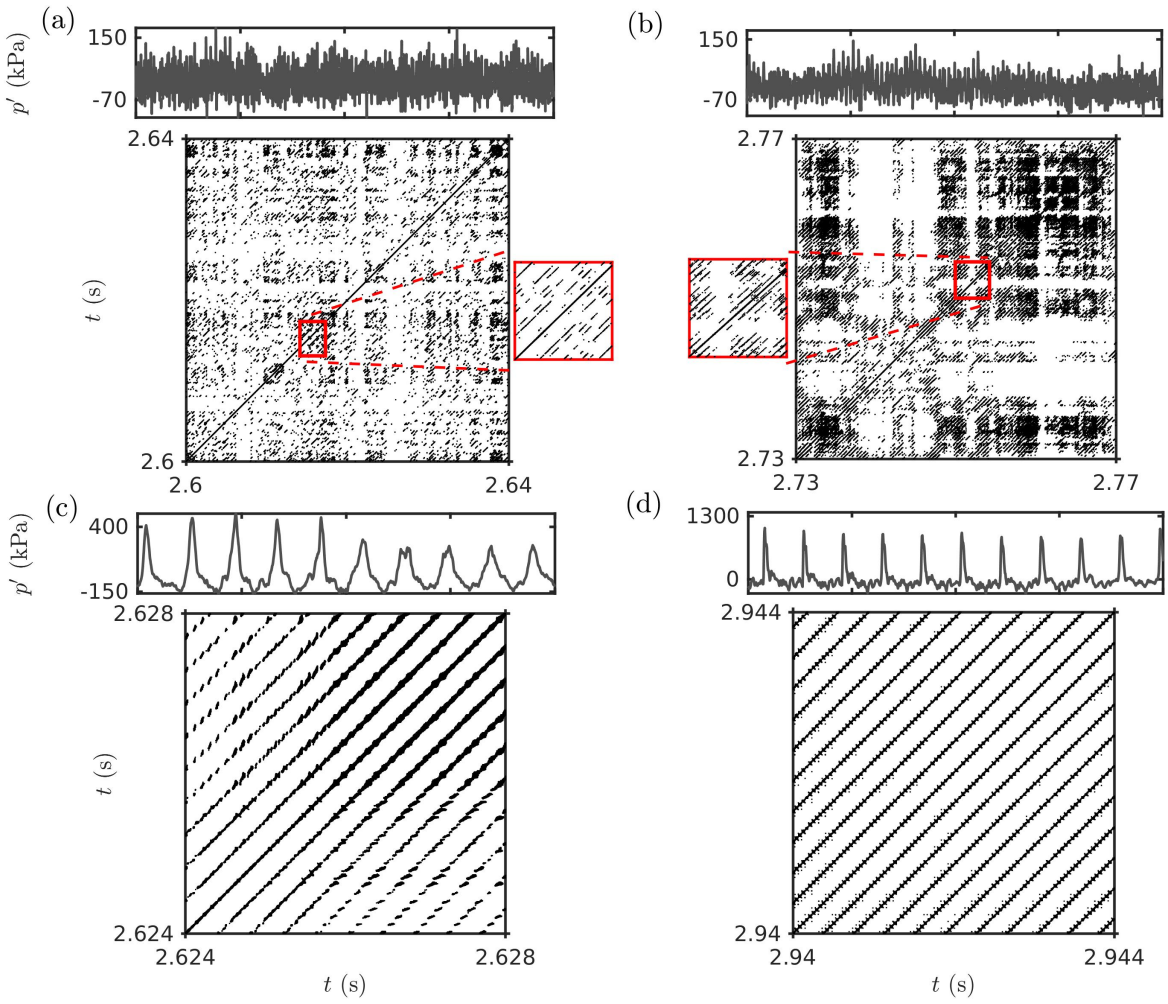

FIG. 8. Recurrence plots (RP) for the dynamics of (a) stable operation (along with a zoomed inset) in Test - A, (b) aperiodic epoch of intermittency (along with its zoomed inset) in Test - D, (c) periodic epoch of intermittency in Test - E, and (d) thermoacoustic instability of Test - E. The recurrence plots are obtained for the corresponding time interval depicted for each dynamical state (a-d) to appropriately detect the patterns. A threshold of 20% of the maximum size of the corresponding attractor is utilized. The parameters such as time delay and embedding dimension are the same as that discussed in Section IVB.

and could possibly suggest chaotic dynamics for the aperiodic oscillations. However, dedicated tests have to be performed before confirming chaotic dynamics. The recurrence plots during periodic oscillations of intermittency (Fig. 8c) and that of thermoacoustic instability (Fig. 8d) show continuous diagonal lines, indicating strong deterministic characteristics in the dynamics. However, during the periodic portion of intermittency, the diagonal lines are

relatively broken due to the gradual decrease in the amplitude of the signal.

E. Multifractal analysis

Many complex signals exhibiting aperiodic oscillations contain certain structural characteristics, which are difficult to be captured by various tools discussed so far. Fractal theory can be used to describe such complex signals that are composed of multiple time scales. By applying fractal analysis to thermoacoustic systems, Nair and Sujith[45] showed that the stable operation (*i.e.*, a state of combustion noise) in a turbulent combustor has multifractal features and these multifractal signatures vanish at the onset of thermoacoustic instability. By following their approach, we study the multifractal behavior of acoustic pressure oscillations observed in the model liquid rocket combustor.

In Fig. 9a, we plot the variation of generalized Hurst exponents with the variation in the order-q for different dynamical states observed during the onset of thermoacoustic instability. We notice that, during stable operation and intermittency, the large scale fluctuations and small scale fluctuations scale differently as the variation of $H(q)$ shows a different trend for both the states. Contrary to this, $H(q)$ shows a negligible change with variation in q during thermoacoustic instability, indicating the existence of single scale during thermoacoustic instability.

Further, we observe a nonlinear variation of the mass exponents, $\tau(q)$, with scaling order q in Fig. 9b for all the states except thermoacoustic instability. Generally, a linear and nonlinear variation of $\tau(q)$ represents monofractal and multifractal behavior of the signal, respectively[69]. This indicates that the states of stable operation and intermittency exhibit multifractal behavior which reduces to a monofractal-like behavior during thermoacoustic instability. Also, the resulting multifractal spectra shown in Fig. 9c for stable operation and intermittency exhibits a wide spectrum spanning several values of singularity exponents (α). Thus, the variation of generalized Hurst exponents, mass exponents, and the multifractal spectrum strongly point out to the presence of multifractal nature in these oscillations.

During thermoacoustic instability, this multifractality is lost. This loss of multifractality is evident from the invariant nature of $H(q)$, the linear variation of $\tau(q)$ with q, and the collapse of the multifractal spectrum to a shorter arc centred around a non-zero α. This non-zero value of α, and the non-integer value of the $H(q)$ further confirms the monofractal-like

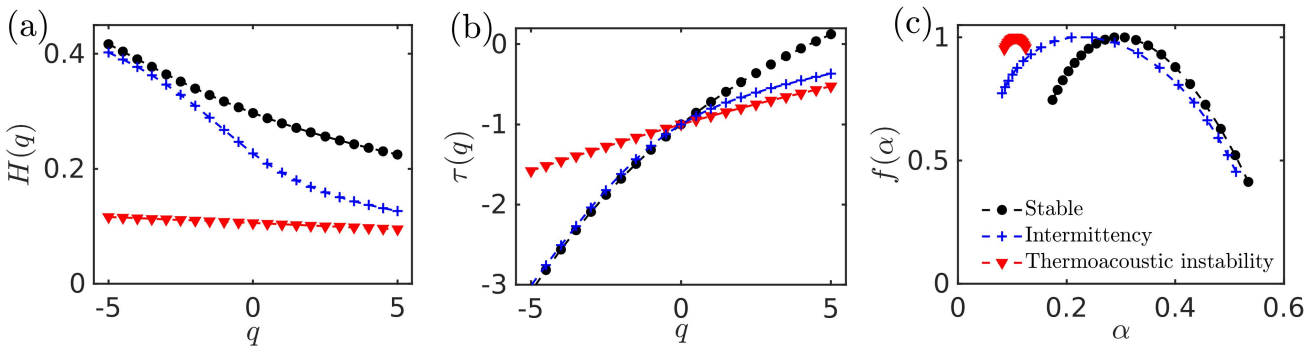

FIG. 9. Multifractal analysis is performed on the stable operation (black) in Test - A, intermittency (blue) in Test - E, and thermoacoustic instability (red) of Test - E. (a) Generalized Hurst exponents, (b) mass exponents, and (c) multifractal spectrum are plotted to characterize the multifractal features of the various dynamics observed in the rocket combustor. The MFDFA method of a third order polynomial fit and a q range of -5 to 5 is used. The window size of 2 - 10 cycles of 2650 Hz oscillations is used, as described in Section IIC.

behavior of acoustic pressure signals during thermoacoustic instability. Such a monofractal behavior for periodic signals have been shown for plasma signals[78].

Additionally, the multifractal spectra during stable operation and intermittency display a right skewed behavior (Fig. 9c). This right skewness suggests that the multifractal dynamics of the pressure oscillations is determined predominantly by the small scale fluctuations. It is also reflected in the reduction in the slope of generalized Hurst exponents for positive order q, indicating that the q^{th}-order root mean square values are insensitive to the local fluctuations with large magnitudes[69]. Having studied the dynamical features of acoustic pressure oscillations during the onset of thermoacoustic instability, now we proceed to quantitatively characterize the dynamical transitions observed in the system dynamics of liquid rocket combustor.

F. Measures to distinguish different dynamical states

We have shown that a thermoacoustic system can exhibit different dynamical states such as stable operation, intermittency, and thermoacoustic instability. A measure which can distinguish between these different dynamical states would be an ideal tool for engineers and simulators to help in assessing the stability of a rocket combustor.

In Fig. 10, we show several measures which exhibit a quantitative change during the transition from stable operation to thermoacoustic instability. In Fig. 10a, we plot the time series of acoustic pressure without removing the mean pressure, during Test - C containing the transition from stable operation to thermoacoustic instability via intermittency, for which the measures are evaluated. The variation of conventional measures employed to detect the transition to thermoacoustic instability such as root mean square value (Fig. 10b), the variance of the oscillations (Fig. 10c), and magnitude of the dominant frequency from the amplitude spectrum (Fig. 10d) are plotted. The entire time series is split into 100 segments of 6 ms interval each for plotting Fig. 10b and Fig. 10c. Due to the compromise in the frequency resolution with shorter window size, we use a relatively larger window interval of 55.6 ms, which resulted in 8 segments of the actual time series, for plotting Fig. 10d.

The variation of both root mean square and variance of the acoustic pressure oscillations increases progressively as the system dynamics approaches thermoacoustic instability. The non-monotonic trend in the variation of these measures prior to thermoacoustic instability is due to the presence of intermittency. The magnitude of the dominant frequency in the amplitude spectrum calculated with a frequency resolution of 18 Hz exhibits a gradual variation from stable operation to thermoacoustic instability. However, to determine the onset of thermoacoustic instability from these measures, an apriori knowledge of the expected amplitude levels out of the combustor is required. Armed with the knowledge of the amplitude levels during the onset of thermoacoustic instability in a combustor, one can determine whether thermoacoustic instability is attained or not. However, in most scenarios, the amplitude levels in a combustor are difficult to predict as they depend highly on the operating conditions, working fluids *etc.* Even if this is overlooked, using these measures, we cannot robustly distinguish the transition between the states of stable operation, intermittency, and thermoacoustic instability.

In an attempt to overcome the shortcomings of these conventional measures, Orth *et al.*[41] introduced the maximum of cross correlation (CC_{max}) as a measure to distinguish between stable operation and thermoacoustic instability. CC_{max}, bounded between -1 to 1, captures the highest similarity between two time series. In Fig. 10e, we show the variation of the maximum value of the cross correlation (CC_{max}) between the acoustic pressure signals acquired at two different locations in the combustor (labelled as 'Fuel Manifold Pressure' and 'Right Wall Pressure' in Fig. 10b). In this study, we find that CC_{max} is unable to

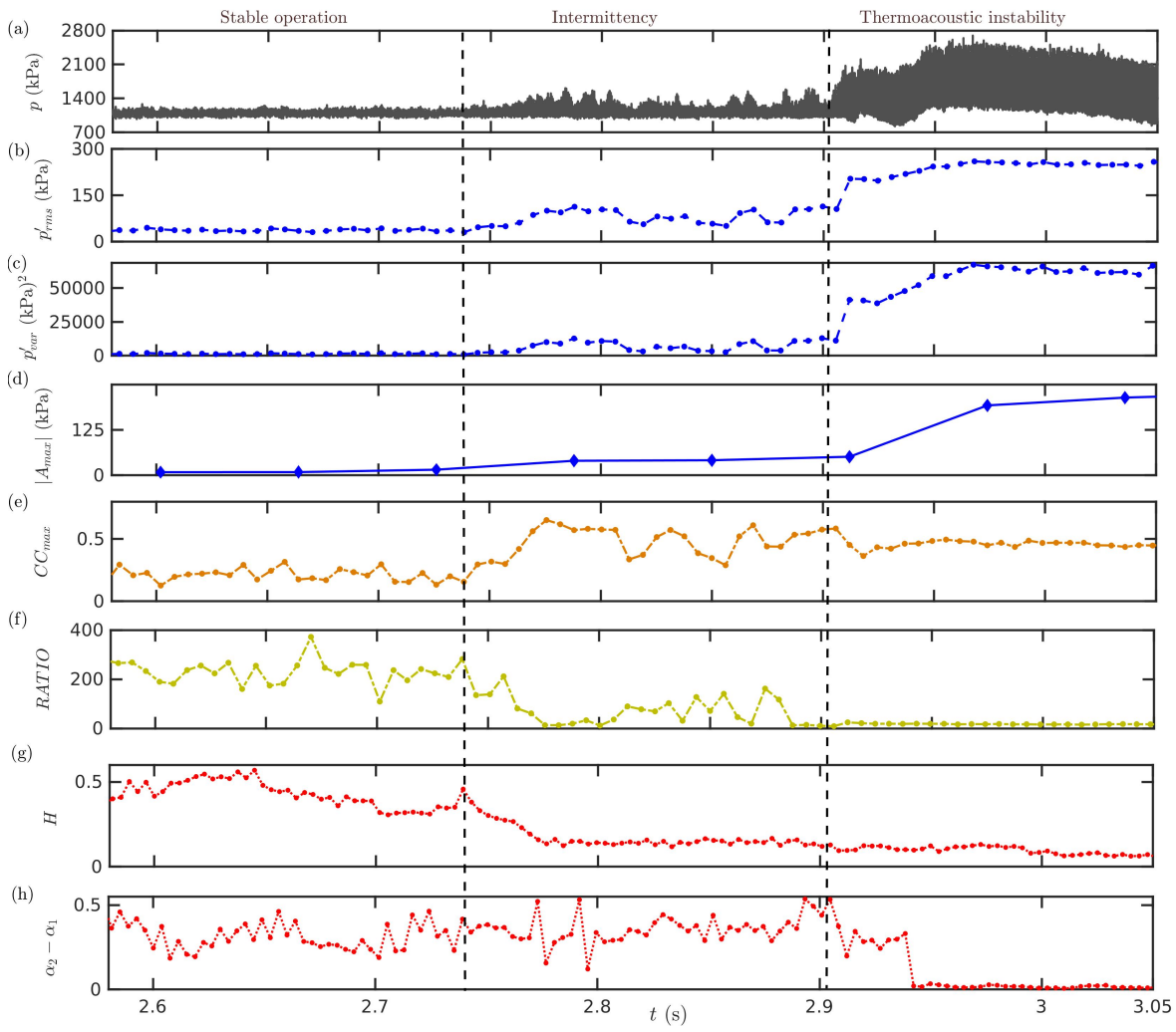

FIG. 10. (a) The time series of acoustic pressure (p) during Test - C containing the transition from stable operation to thermoacoustic instability via intermittency. The variation of (b) root mean square value (p'_{rms}), (c) the variance of the oscillations (p'_{var}), (d) the magnitude of the dominant frequency from the amplitude spectrum ($|A_{max}|$), (e) maximum of cross correlation (CC_{max}), (f) ratio of determinism to recurrence rate ($RATIO$), (g) Hurst exponent (H), and (h) multifractal spectrum width ($\alpha_2 - \alpha_1$) are plotted to distinguish the dynamical transitions across stable operation, intermittency, and thermoacoustic instability. The dashed vertical lines demarcating the three dynamical states are marked by visual inspection.

distinguish between intermittency and thermoacoustic instability as the values of CC_{max} are nearly the same during intermittency and thermoacoustic instability. Next, we show the variation in the recurrence based measure: the ratio of determinism to recurrence rate

($RATIO$) in Fig. 10f. We note that the value of $RATIO$ starts decreasing with the onset of intermittency and decays to almost zero during thermoacoustic instability. CC_{max} and $RATIO$ are plotted for a window size of 7.5 ms corresponding to 20 cycles of oscillations.

Finally, the variation of fractal measures, Hurst exponent (H) in Fig. 10g and multifractal spectrum width (α_2 - α_1) in Fig. 10h are plotted to distinguish the dynamical transitions across stable operation, intermittency, and thermoacoustic instability. Here, α_2 and α_1 are the extreme values of the singularity exponents covered by the multifractal spectrum. The multifractal spectrum width (α_2 - α_1) is calculated by measuring the range of singularity exponents covered by the spectrum. For the multifractal measures, a window size of 37.6 ms corresponding to 100 cycles of oscillations with an overlap of 90 cycles is used. The multifractal spectrum width drops from near 0.4 to lower than 0.02 during the onset of thermoacoustic instability. However, the presence of intermittency cannot be detected by this measure. The value of Hurst exponent (H) varies from around 0.5 during stable operation to less than 0.1 during the onset of thermoacoustic instability. During intermittency, if the value of H drops below 0.1, this model rocket combustor can be considered to be in the proximity of an impending thermoacoustic instability. However, the critical Hurst exponent below which thermoacoustic instability is imminent may vary from system to system. Hence, $RATIO$, Hurst exponent, and multifractal spectrum width collectively can be used to distinguish the combustor operation across all three states for a rocket combustor, as they possess fixed values for a particular type of dynamics, unlike traditional measures such as rms value, amplitude of frequency peaks, and variance of the oscillations.

Next, in Fig. 11, we show that the same measure $RATIO$ can also be used to detect the transitions from aperiodic to periodic oscillations, and vice versa, in a signal (see Fig. 11a). We compare the efficacy of $RATIO$ as compared to CC_{max} in detecting such transitions. We also show the variation of DET and RR in Fig. 11c,d, respectively. We observe that through a windowed variation of CC_{max} (Fig. 11b) and $RATIO$ (Fig. 11e), we can detect the switching between periodic and aperiodic behavior during intermittency. Here, CC_{max} is obtained by cross correlating the same two pressure signals used to calculate CC_{max} plotted in Fig. 10. Zoomed views of the normalized pressure time series of the two signals ($p'_{n,fuel}$ and p'_n) are plotted for an aperiodic epoch of intermittency, a periodic epoch of intermittency, and thermoacoustic instability in Fig. 11i-iii. A window size of 2.3 ms corresponding to two hundred slices of the actual time series is used to calculate all measures in Fig. 11. A

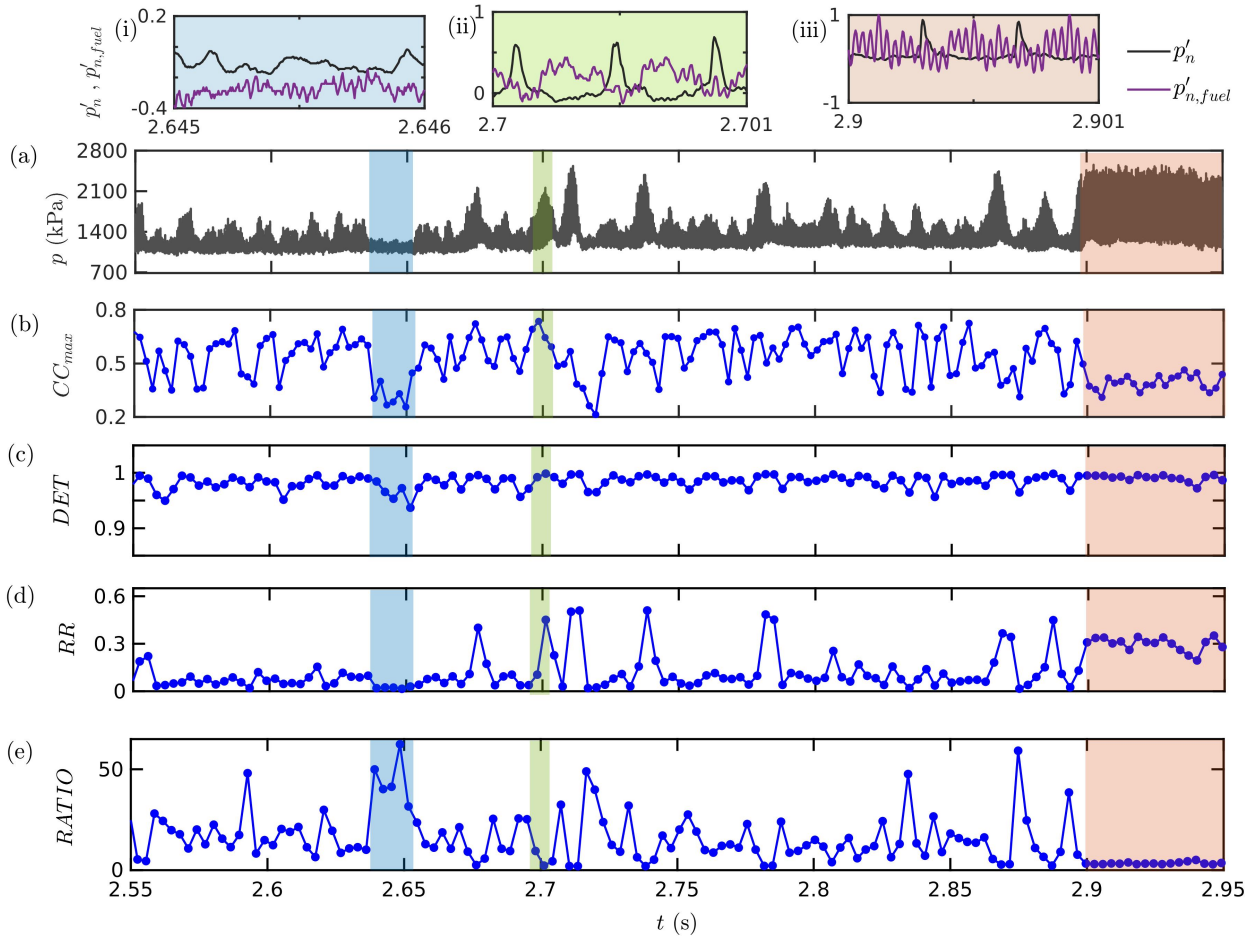

FIG. 11. The time series of (a) acoustic pressure (p) is plotted during the transition from intermittency to thermoacoustic instability for Test - E. The variation of (b) maximum of cross correlation (CC_{max}), (c) determisim (DET), (d) recurrence rate (RR), and (e) ratio of determinism and recurrence rate ($RATIO$) to detect the aperiodic to periodic transitions, and vice versa. The blue shaded region corresponds to the long aperiodic epoch of intermittency, the greeen shaded region corresponds to the periodic epoch of intermittency, and the red shaded region corresponds to the epoch of thermoacoustic instability. Zoomed views of normalized pressure signals at the right wall (p'_n) and fuel manifold ($p'_{n,fuel}$) locations are shown for (i) aperiodic epoch of intermittency, (ii) periodic epoch of intermittency, and (iii) thermoacoustic instability, respectively.

smaller window size is necessary to detect the aperiodic-periodic transitions. DET, RR and subsequently, $RATIO$ are obtained by calculating the recurrences of the phase trajectories within a threshold of 20% of maximum size of the corresponding attractor. The time delay and embedding dimension are calculated for the entire time series and are found to be 0.196

ms and 10, respectively.

We observe an uncharacteristically higher value of DET for the aperiodic oscillations, compared to other combustors[79]. The value of DET for both aperiodic and periodic dynamics in this data (see Fig. 11c) remains nearly the same. The value of $DET \sim 1$ suggests the possibility of high deterministic features[77] in the aperiodic oscillations of the rocket combustor dynamics. This high determinism value could be a result of the dynamics of the flame front, arising from the globally unstable hydrodynamic field.

On the other hand, the value of RR exhibits a significant increase during the transition from aperiodic to periodic oscillations (see Fig. 11d). Hence, $RATIO$ exhibits a higher value for aperiodic oscillations and lower value for periodic oscillations. On the other hand, for CC_{max}, we expect a value close to 0 for aperiodic oscillations with low similarity and a higher value close to 1 for periodic oscillations with large similarity. The blue and green shaded regions in Fig. 11a-e represents an aperiodic epoch and a periodic epoch, respectively during intermittency. During the aperiodic epoch, we observe that CC_{max} shows lower values while $RATIO$ exhibits larger values. We observe the opposite behavior in both $RATIO$ and CC_{max} during the periodic epoch of intermittency. During thermoacoustic instability (see red shaded region in Fig. 11a-e), the values of both these measures are largely invariant, denoting sustained periodic behavior in the system. For this state, we observe that the values of both CC_{max} and $RATIO$ are low. The lower value of CC_{max} is unexpected during thermoacoustic instability as the dynamics during this state is periodic.

The reason behind the lower value of CC_{max} for both periodic and aperiodic oscillations can be understood from the overlapped plot of the two pressure signals used for the calculation of CC_{max} (see Fig. 11i-iii). To aid us in detecting the similarity, the two time series ($p'_{n,fuel}$ and p'_n) are normalized. For the aperiodic epoch of intermittency, we do not observe any similarity between the two signals (Fig. 11i). During the periodic epoch of intermittency (Fig. 11ii), we observe that the two signals follow a nearly similar trend at a finite non-zero time lag, leading to higher values in CC_{max}. On the contrary, during the state of thermoacoustic instability (Fig. 11iii), we notice that the time series of $p'_{n,fuel}$ contains significantly higher frequencies, whereas that of p'_n contains lower frequency corresponding to fundamental mode of the combustor (2650 Hz). This difference in the oscillations of acoustic pressure at different locations contribute to lower the value of CC_{max}. Unlike CC_{max}, we observe that the lower values of $RATIO$ correctly captures the periodic oscillations during thermoacous-

tic instability as well as during intermittency. This suggests that using $RATIO$ is better than CC_{max} to unambiguously determine the periodic-aperiodic-periodic transitions in the acoustic pressure signal observed during the onset of thermoacoustic instability. We also remark that RR can be a good candidate to distinguish the aperiodic-periodic transitions if there is a significant variation in RR during the aperiodic-periodic transitions.

IV. SUMMARY

The dynamics of acoustics pressure oscillations during the transition from stable operation to thermoacoustic instability in a model multi-element rocket combustor is analyzed. We observe that the transition from small amplitude stable operation to large amplitude thermoacoustic instability occurs through intermittency. Intermittency is a dynamical state wherein bursts of high amplitude periodic oscillations exist amidst epochs of low amplitude aperiodic oscillations, distributed in a seemingly random manner. The waveform during thermoacoustic instability is highly nonlinear, consisting of typically steepened pressure wavefronts leading to the formation of shock waves, and is significantly different from the sinusoidal limit cycle oscillations typically seen in gas turbine combustors. As a result, we obtain a characteristic trefoil knot like shape of the phase space attractor during thermoacoustic instability. Further, we detect the dynamical switching between period-3 and period-4 oscillations in an apparently random manner during thermoacoustic instability and the periodic epochs of intermittency. Such complex limit cycle dynamics are seldom seen in gas turbine combustors.

Through a suitable multifractal analysis, we detect the collapse of multifractality during the onset of thermoacoustic instability. We present a recurrence based measure ($RATIO$) and two fractal based measures (multifractal spectrum width and the Hurst exponent), that can be used to distinguish between different states of combustor operation. We found that these measures are more robust than the existing measures such as root mean square of the oscillations, amplitude, maximum of cross correlation *etc.* in distinguishing the dynamical state of a rocket engine. The measures illustrated in this study can be used to validate the CFD multi-fidelity simulations used for optimizing the stability and performance metrics of the rocket combustor. Such an approach can reduce the developmental timescales of a rocket engine. Summarizing, the signals pertaining to rocket combustors are different from their

gas turbine counterparts and other derived laboratory combustors due to the significant contribution of nonlinearities in the rocket combustor. Hence, extreme care must be exercised while extending the results obtained for gas turbine combustors to rocket combustors.

CHAPTER 3
RECURRENCE ANALYSIS OF ACOUSTIC PRESSURE OSCILLATIONS

I. INTRODUCTION

Rhythmic beating of heart[80], periodic firing of neurons[81], spontaneous oscillations of chemical reactions[82], dangerous self-excited oscillations in suspension bridges[83] and aircraft engines[84] are a few examples of the countless periodic phenomena we come across in our lives. Most of these phenomena exhibit oscillations at a preferred timescale, known as the time period of the oscillation. However, certain periodic phenomena are inherently made up of more than one timescale in an oscillation[85]. Such periodic phenomena are popularly classified as slow-fast oscillations[85]. Such systems are found across a wide range of applications ranging from medicine[86], economics[87], physical sciences[88] to engineering[89–91].

For an example, let us consider the electrocardiogram (ECG) signal wherein the electrical activity in the heart is recorded using a set of electrodes. A typical cycle of ECG signal is defined by different processes such as atrial depolarization, ventricular depolarization, and ventricular repolarization[92]. Each of these processes (designated as P wave, QRS complex, and T wave in one cycle of the ECG signal) have an intrinsic timescale. Using multifractal analysis on ECG signals, physiologists have successfully distinguished between healthy and unhealthy individuals[93]. A characteristic feature of slow-fast systems is that their periodic waveforms are radically different from those of harmonic oscillators. For the most simple case of a slow-fast system containing two timescales, a slow growth/decay is accompanied by a fast decay/growth. As a result, a slow-fast system could spend more time in the growth or decay phase. To present an example in electrical engineering, the charge and discharge of a capacitor[94] is characterized by a slow and fast timescale, respectively. In a similar manner, the periodic stick-slip motion of a bowed violin string exhibits more than one timescale[95].

In nonlinear dynamics literature, the nomenclature of slow-fast systems have also been used to describe the multiple timescales that cause periodic amplitude modulation, bursting oscillations, and mixed-mode oscillations[96]. Periodically modulated waves are crafted by a slow periodic amplitude modulation over a fast oscillating signal. On the other hand, mixed-mode oscillations are periodic oscillations which exhibit amplitude switching between

two or more amplitude states. Bursting oscillations are characterized by epochs of large amplitude periodic oscillations followed by quiescence[97]. In these type of slow-fast systems, the slow timescale corresponds to the modulation of the envelope of the signal while the fast timescale pertains to the high frequency oscillation in the signal. However, unlike all these types of periodic oscillations where the rate of evolution of the signal over one time period remains the same, the slow-fast systems described in this study contain all the slow and fast timescales within one period of the oscillation. Such slow-fast systems have been long studied under the guise of relaxation oscillators. These oscillators are a class of limit cycle oscillators, that are characterized by a non-sinusoidal periodic waveform[98]. Relaxation oscillations have been modelled using several models such as the Van der Pol oscillator[98], Fitz-Hugh-Nagumo oscillator[99], and LEGION[100].

Traditionally, slow-fast systems with a pre-established set of governing equations have been solved using conventional methods from linear theory. A classical technique is to reduce the set of governing equations to the weak or the strong nonlinear limit[101], whenever the two timescales are widely separated. Then, the system of equations is solved to obtain the resultant amplitudes and phases of the signal. Apart from this method, various other techniques such as perturbation theory, method of multiple timescales, and averaging exists[59]. However, experimental and other real-world signals rarely have any well-defined functional forms, which can be solved using these methods. Moreover, the timescales in practical systems are seldom widely separated. All these obstacles render the analysis of such signals intractable. At this juncture, the framework of dynamical systems theory and complex systems theory offers a promising way to understand and characterize the dynamics of complex systems in man-made systems as well as nature[102,103].

In this study, we characterize the dynamics of slow-fast oscillations observed in synthetic periodic slow-fast signals obtained from well-established models, i.e., Van der Pol, a modified form of Izhikevich model, and the Hodgkin-Huxley model. We use methods based on recurrence analysis of the phase space trajectory such as recurrence plot (RP) and recurrence network (RN) to distinguish the properties of these signals. The periodic nature of the signals attributes a closed loop structure to the RN and a continuous diagonal line in the RP. In addition to this, we observe additional features such as clustering and protrusions on the topology of RN for slow-fast systems. These structures exhibit a clear departure from the ring topology in the RN for regular sinusoidal signals. Thus, we argue

that these clustering and protrusion effects in RN arise due to the presence of the multiple timescales in an oscillation of the signal. Furthermore, in the RP of these signals, we detect the existence of characteristic micro-patterns along the diagonal lines. Following the same methodology, we analyze two high-dimensional periodic slow-fast signals of thermoacoustic oscillations from experiments: the time series of heat release rate signal from a model gas turbine combustor[104], and the acoustic pressure signal obtained from a model liquid rocket combustor[41].

The rest of the paper is outlined as follows. The methodology used in this study is briefly described in Section II. Here, we concisely detail the RP and RN construction technique adopted in this study. Next, in Section III, we begin by analyzing low-dimensional systems and comparing with a single timescale signal (sine wave). Later, we extend the analysis for probing slow-fast dynamics in high-dimensional real-world signals. Finally, we summarize the key findings in Section IV.

II. METHODOLOGY

Many real-world signals exhibit different dynamics such as limit cycle, chaos, mode-locking, quasiperiodicity, and amplitude switching, which can be explained from their nonlinear behavior. Using tools from dynamical systems theory, the occurrence of such behaviors across a wide range of systems have been understood[101]. The dynamics of such nonlinear systems can be visualized by plotting the corresponding phase space[57]. Each point on the phase space trajectory is described as a unique combination of system variables. However, for physical systems and in experiments, it is almost impossible to acquire all the pertinent system variables to construct the phase space trajectory.

To circumvent this problem, Takens introduced the method of phase space reconstruction by time delay embedding[57]. In this method, the phase space is realized by plotting the time series against its delayed versions in an appropriate dimensional space. The optimum time delay and the embedding dimension need to be selected prior to phase space reconstruction. The time delay (τ) is selected such that the delayed vectors are independent of each other. Using autocorrelation function[59] (ACF), we can estimate τ. Then, we can use the modified false nearest neighbor method developed by Cao[60] to obtain the optimum embedding dimension (d).

Using this method of phase space reconstruction, we can visually unravel the dynamics of nonlinear systems from its phase space attractor only in low dimensions ($d \leq 3$). However, a vast number of real-world signals usually tend to have higher optimum embedding dimensions ($d > 3$). As a result, the fundamental property of recurrence of phase space trajectory is exploited to understand the underlying hidden features of high-dimensional nonlinear systems[61,77].

A. Recurrence plots

Recurrence of phase space trajectory is a fundamental property of deterministic signals. Recurrence plots (RP), introduced by Eckmann *et al.*[61], allows us to identify the time instants at which the trajectory of a system roughly revisits the same area in a d-dimensional phase space. To appropriately construct a RP, we need to estimate the optimum time delay (τ) and the embedding dimension (d), beforehand.

For a time series $x(t)$ of length n, the pairwise distances between state points in the reconstructed phase space can be contained in a distance matrix (D_{ij}), as formulated below.

$$D_{ij} = \|x_i - x_j\| \quad i, j = 1, 2, \ldots, n - (d-1)\tau. \tag{11}$$

Here, $\|x_i - x_j\|$ is the Euclidean distance between the two state points, i and j, on the reconstructed phase space trajectory. Next, the distance matrix is binarized by defining a threshold (ϵ) to obtain the recurrence matrix[105] (R_{ij}).

$$R_{ij} = \Theta(\epsilon - D_{ij}), \tag{12}$$

where, Θ is the Heaviside step function and ϵ is the threshold defining the neighborhood around the state point. One of the method to select a recurrence threshold is to fix a recurrence rate[77] (RR). RR is defined as the percentage of recurring points in a RP. We observe that a value lower than the optimum RR fails to completely capture the periodicity in the signal and is reflected as broken diagonal lines in the RP. A value higher than the optimum value results in superfluous connections in the RN, distorting the phase space topology. In this study, an optimum value of RR is selected after careful consideration for each slow-fast system.

Whenever the phase space trajectory recurs within the region defined by the ϵ-size ball, it is marked as a black point while non-recurring points are marked as white points in the RP. In the recurrence matrix, one and zero are designated for black point and white point, respectively. Thus, a RP is a two-dimensional arrangement of black and white points that exhibits different patterns characterizing different dynamics of the signal. Patterns in RPs have garnered the attention of physicists in many instances[106–108]. However, understanding such patterns in the RPs of slow-fast systems have not yet been probed, to the best our knowledge.

RPs have found application in life sciences, engineering, earth sciences, physics, economics, social sciences, and sports science[77,109,110]. From the patterns in the RPs constructed for a time series of heartbeat interval signal, cardiologists have been able to distinguish life threatening arrhythmia from less severe cardiac disorders[105]. Similarly, RPs constructed for the time series of acoustic pressure oscillations have been used to distinguish between safe and dangerous operational modes in fluid mechanical systems[46,111–113]. The method of RPs have been extended to cross recurrence plots to explain synchronization between oscillators[114]. Further, statistical measures can be derived from the organization of such black and white points in the RPs. Such an analysis is known as the recurrence quantification analysis. For a detailed review on recurrence methods, we refer the readers to Webber & Marwan[63].

B. Recurrence networks

In nature as well as engineering examples, there exist many instances where a system is a collection of several interconnected subsystems, necessitating the entire system to be studied as a whole rather than a sum of its parts. Such systems are classified as complex systems[115]. The interaction between the various subsystems in the complex system leads to an emergence of collective behavior, self-organization etc. The framework of complex networks allows one to account for the nonlinear interaction between the different subsystems in a complex system. A complex network is comprised of nodes representing the components of the system and edges which represent the interaction between the components. Recurrence networks[116] are a class of complex networks through which high-dimensional systems can be understood. Similar to the RPs, we can create a ϵ-RN[116], where ϵ is the threshold. The phase space of

the high-dimensional nonlinear system is preserved in the topology of the RN[52].

To construct a RN from the time series, we require an adjacency matrix A, to be computed from the recurrence matrix R for an ϵ-threshold.

$$A_{ij} = R_{ij} - \delta_{ij} \tag{13}$$

where δ is the identity matrix of same size as R. The adjacency matrix A provides information about the nodes which are connected in the RN. For $A_{ij} = 1$, the nodes are connected only when the state space vector is within the ϵ-threshold. If $A_{ij} = 0$, the nodes remain disconnected. Unlike the RP, several network measures quantifying the geometrical structure of the phase space attractor can be computed from a RN[116,117].

Using the network properties obtained from the RN, a number of studies have used RN to study diverse systems. Gao *et al.*[118] distinguished the dynamical behavior of stratified flows. Using a suitable RN for a thermoacoustic system, Godavarthi *et al.*[52] captured the topological differences in RN as the system undergoes various dynamical transitions. The measures derived from RN have the capability to indicate early warning of oscillatory instability[48,52] and detecting synchronization properties of coupled oscillations[53]. Gotoda *et al.*[119] showed the presence of small-world nature in the ϵ-threshold RN in a turbulent combustor close to flame blowout. Using measures from RN, Ávila *et al.*[120] predicted the occurrence of preeclampsia, a pregnancy-specific disorder. George *et al.*[121] classified binary stars based on the measures such as characteristic path length and average clustering coefficient, computed from the corresponding RN.

In this study, we reconstruct the phase space by time delay embedding, and compute the RPs, and the RNs based on an optimum value of RR as recurrence threshold to analyze the dynamics of different slow-fast systems.

Each node in the RN is color coded based on a network property known as degree[122]. Degree refers to the number of connections a node has to other nodes in the network. Degree (D) of a node i is calculated as,

$$D_i = \sum_{j=1}^{N} A_{ij} \tag{14}$$

where NxN is the size of A_{ij}. Finally, we visualize the RN using the open-source network analysis platform, Gephi[123].

III. RESULTS AND DISCUSSIONS

We progressively investigate the recurrence properties of slow-fast system from low-dimensional systems to high-dimensional systems. For the low-dimensional system, we consider the Van der Pol oscillator, a modified signal derived out of Izhikevich's spiking neuron model[124] and the Hodgkin-Huxley model[81,125]. We, then, analyze the time series of heat release rate oscillations obtained from experiments in a gas turbine type laboratory-scale turbulent combustor[104] and the acoustic pressure signal from a laboratory-scale model multi-element liquid rocket combustor[41], during the state of thermoacoustic instability, to understand the recurrence dynamics of slow-fast systems in higher dimensions.

A. Recurrence analysis of low-dimensional models

Prior to understanding slow-fast systems, we analyze a harmonic signal, namely a sine wave of amplitude unity and frequency $\frac{1}{2\pi}$ Hz (see Fig. 1a), which is a definite single timescale system in its phase space. In Fig. 1b, we observe that the phase space of the sine wave is a circular loop structure wherein the phase space trajectory evolves at a uniform speed. Here, uniform speed of the phase trajectory is attributed to successive state points on the trajectory separated by equal distances in the phase space. In the corresponding RP (see Fig. 1c), we observe only equally spaced diagonal lines corresponding to the time period of the oscillation. The corresponding RN topology of the sine wave (see Fig. 1d) shows a circular loop filled up with same degree nodes.

Now, we start analyzing slow-fast systems where we first consider the Van der Pol system[98], which is perhaps the most studied slow-fast system. The governing equations of the Van der Pol system are given below.

$$\begin{aligned} \dot{x} &= \mu(y + x - \tfrac{x^3}{3}), \\ \dot{y} &= -\tfrac{1}{\mu}x, \end{aligned} \tag{15}$$

where, μ is referred to as the nonlinearity parameter used to get relaxation type oscillations. We fix the value of $\mu = 2$ for the current analysis. The time series of variables, $x(t)$ and $y(t)$ of the Van der Pol system are plotted over one another in Fig. 2a. The corresponding phase portrait, shown in Fig. 2b, exhibits a closed loop confirming the periodicity of the time series. However, unlike the phase space of the harmonic signal in Fig. 1b, we observe

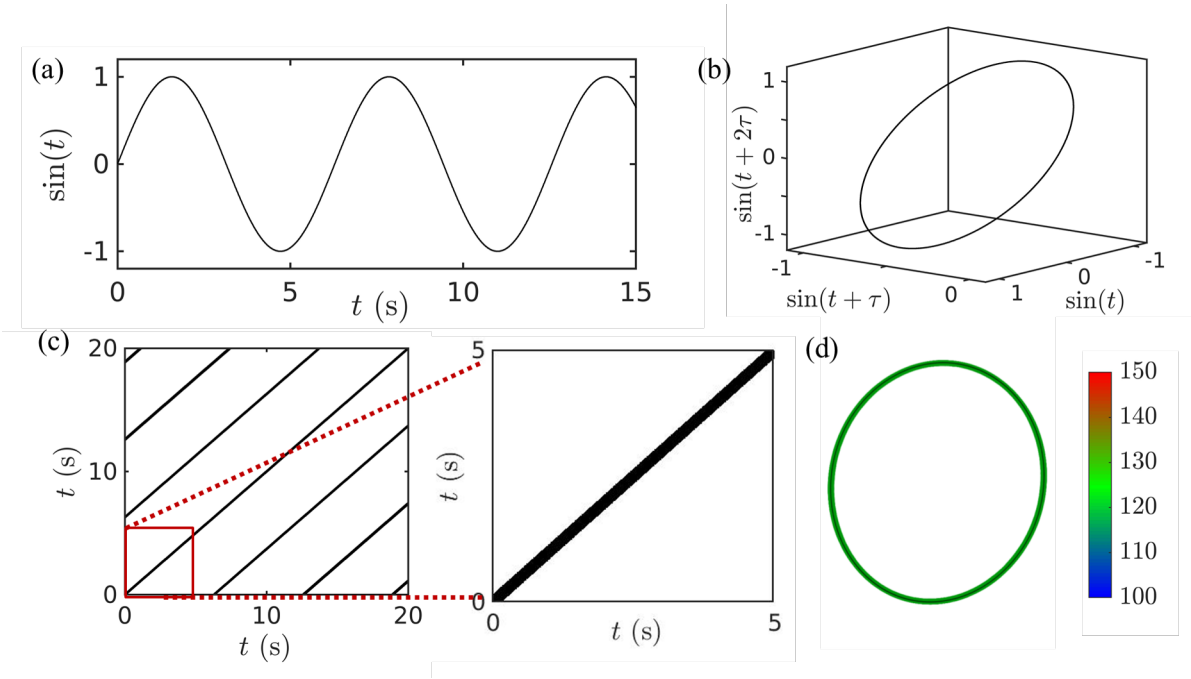

FIG. 1. (a) The time series of sine wave of unit amplitude and time period 2π seconds and amplitude 1 unit, sampled at 100 samples per second. (b)-(d) The corresponding reconstructed phase space calculated for $\tau = 157$, RP along with a zoomed view, and RN, respectively.

that the phase space evolves at different speeds, giving rise to the slow and fast timescales in the evolution of the phase space trajectory. The separation between successive phase space points during the fast epoch is large as compared to that of the slow epoch. As a result, the fast epoch can be visually discriminated from the slow epoch in the phase space. For the Van der Pol system, we observe two epochs of slow oscillations (marked as S) and two epochs of fast oscillations (marked as F) within a cycle in the original phase space (i.e. a plot between the variables x and y of the system).

In Fig. 2c, we show the time series of variable $x(t)$ and its delayed copy $x(t+\tau)$, as required for the reconstructed phase space determined by Takens' delay embedding theorem. Here, the delay τ is obtained by the first zero crossing in the autocorrelation function (ACF). Unlike the original phase space shown in Fig. 2b, in the reconstructed phase space of x by time delay embedding (see Fig. 2d), we obtain four epochs of slow and fast oscillations (marked as S and F, respectively) within a cycle of oscillation. This exercise shows that systems containing slow-fast timescales need to be interpreted carefully based on the technique of phase space reconstruction since the number of slow/fast regions could be exaggerated than

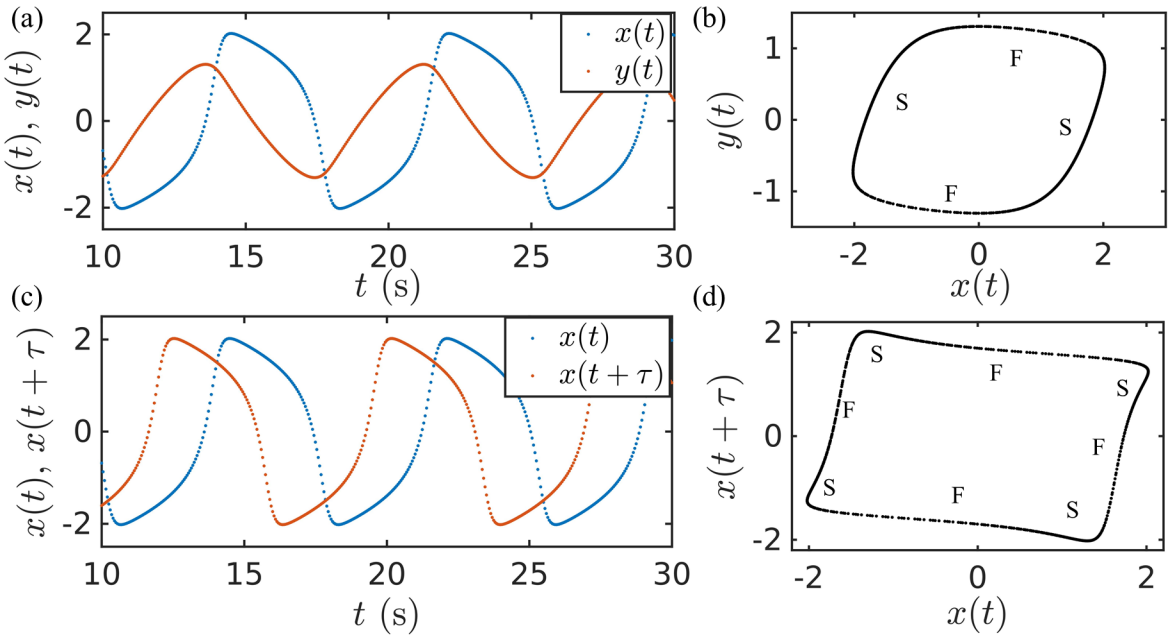

FIG. 2. (a) The time series of x and y of the Van der Pol system for $\mu = 2$. (b) The original phase space between x and y. (c) The time series of x and its delayed copy, $x(t+\tau)$. (d) The reconstructed phase space of x using Takens' delay embedding theorem. S and F indicate the slow and fast motion in the phase space, respectively.

that is present in the original phase space. The reconstructed phase space of $y(t)$ evolves at a single timescale (not shown here) and hence, does not exhibit slow-fast features.

Further, we plot the RP and the corresponding RN for the Van der Pol system in the original phase space and in the reconstructed phase space (see Fig. 3). The recurrence matrix is built by fixing $RR = 0.05$. For both the RPs, (shown in Fig. 3a,c), we observe only diagonal lines, indicating periodic behavior of the system. In the corresponding zoomed view of the RP in Fig. 3(a,c), we observe the presence of momentary thick regions along the diagonal lines of a RP. We attribute these thick regions to slow epochs while the thin regions to the fast epochs in the evolution of the phase space trajectory. We refer to the presence of such distinct black patterns on the diagonal lines in a RP of the periodic signal as micro-patterns of RP. Thus, with the identification of such micro-patterns, we can distinguish the time instances corresponding to slow regions from the fast regions in the signal.

The reason behind the occurrence of such a micro-pattern in the RP can be understood from the evolution of the phase space at slow and fast timescales. When the phase space

trajectory evolves at a slower rate in the phase space, it spends relatively more time within the ϵ-threshold as compared to the phase space trajectory for the fast motion. This leads to the thickening of the diagonal lines in the RP. A similar argument can be given to explain the thinning of the diagonal lines whenever the phase space trajectory exhibits fast motion.

We observe that the network topologies of both the original and reconstructed Van der Pol system are similar to the corresponding phase space observed in Fig. 2(b,d). In the corresponding RNs (see Fig. 3(b,d)), we observe distinct regions which exhibit clustering of high degree (red) nodes amongst the almost uniform distribution of low degree (blue) nodes. The clusters of high degree nodes within a cycle represent the region in which the trajectory moves slowly in the phase space, resulting in more number of connections in the RN. There are two such regions in the RN constructed from the original phase space (see Fig. 3b) and four slow regions in the RN from the reconstructed phase space (Fig. 3d); exactly matching their respective phase spaces in Fig. 2(b,d). Thus. as expected, RN conserves the topology of the original phase space of the signal[126].

Next, we consider another synthetic periodic slow-fast signal (see Fig. 4a) obtained by modifying the time series of variable x obtained from Izhikevich's spiking neuron model[124]. First, we solve for the variable x in the set of equations, shown in Eq. 16. The parameters $a = 0.1$, $b = 0.2$, $c =$ -60, $d = 8$, and $I = 110$ are used to obtain spiking behavior in $x(t)$. Then, the resulting time series is modified, so that enough number of points are present both during the growth and decay phase of the oscillations, to get a connected RN.

$$\begin{aligned} \dot{x} &= 0.04x^2 + 5x + 140 - y + I \\ \dot{y} &= a(bx - y) \end{aligned} \tag{16}$$

We observe that one oscillation in this signal is almost symmetric about the growth and the decay phase (Fig. 4a). The reconstructed phase space using $\tau = 102$ data points (obtained from ACF) for this synthetic signal is plotted in Fig. 4b. We observe that the three-dimensional phase space attractor is stretched along the three axes, while maintaining a closed loop structure in the evolution of the phase space trajectory for one oscillation of the periodic signal.

The RP for this synthetic signal is plotted in Fig. 4c. We observe that the RP exhibits continuous equispaced diagonal lines, signifying the periodic dynamics of the signal. On top of this, the micro-patterns in the RP exhibit intricate features unique to slow-fast systems. Similar to the Van der Pol system, the thickened portions of the diagonal line (see Fig. 4c)

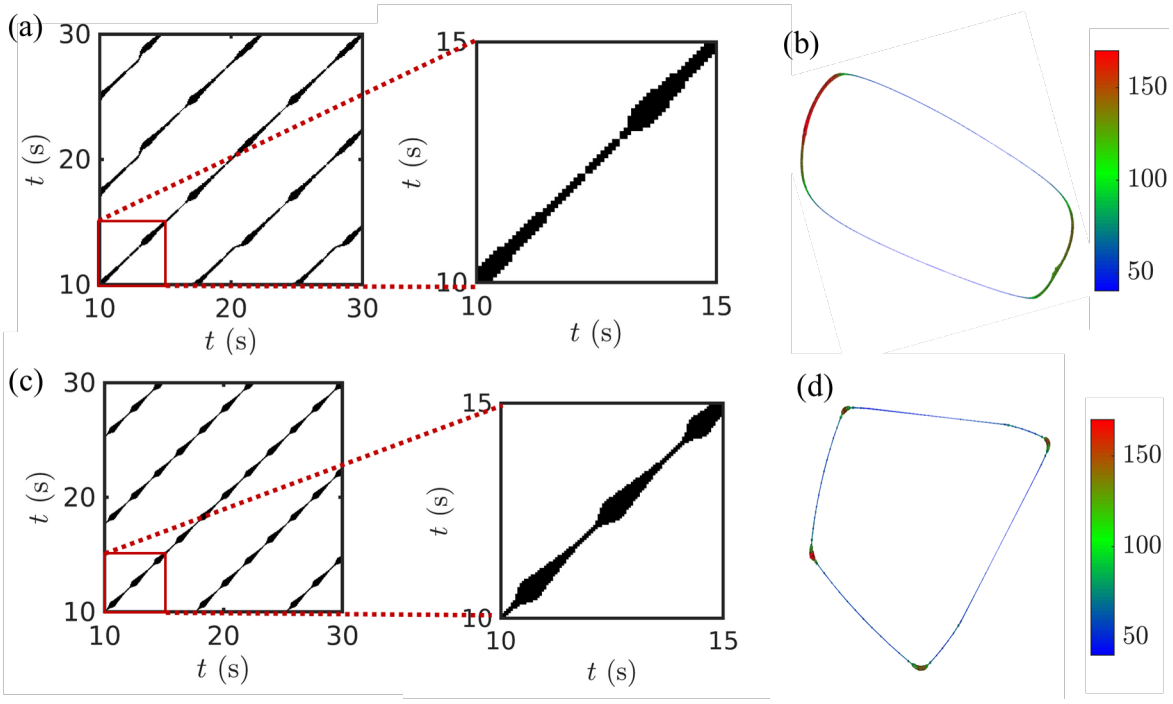

FIG. 3. (a) RP along with its zoomed view and (b) the corresponding RN constructed using the original variables x and y of the Van der Pol oscillator, shown in Fig. 2. (c,d) The same plots are shown for the phase space reconstructed using time delay embedding for the variables $x(t)$ and $x(t+\tau)$. The nodes in RN are color coded based on their degree. A recurrence threshold of $RR = 0.05$, d=2, and τ=39 are used.

correspond to the slow motion in the phase space. In addition, the line segments perpendicular to the diagonal line in the RP pertain to the fast motion of the phase space trajectory. A perpendicular line segment occurs amidst two thickened regions along the diagonal line in the RP whenever the phase space trajectories traversing in opposite directions are spaced within the ϵ-threshold. This is also confirmed by the fast motions of the phase space trajectory at the extremities (or) corners of the phase space in Fig. 4b, where the phase space trajectory reverses direction abruptly. Hence, the small line segments perpendicular to the main diagonal line pertain to the fast motion in the phase space. Here, we remark that there is no such occurrence of two close phase space trajectories traversing in opposite directions in the Van der Pol system (see Fig. 2c,d). As a result, we do not obtain any perpendicular lines in the RP of the Van der Pol system.

In Fig. 4d, the RN for this synthetic signal is plotted. Within one cycle, the trajectory

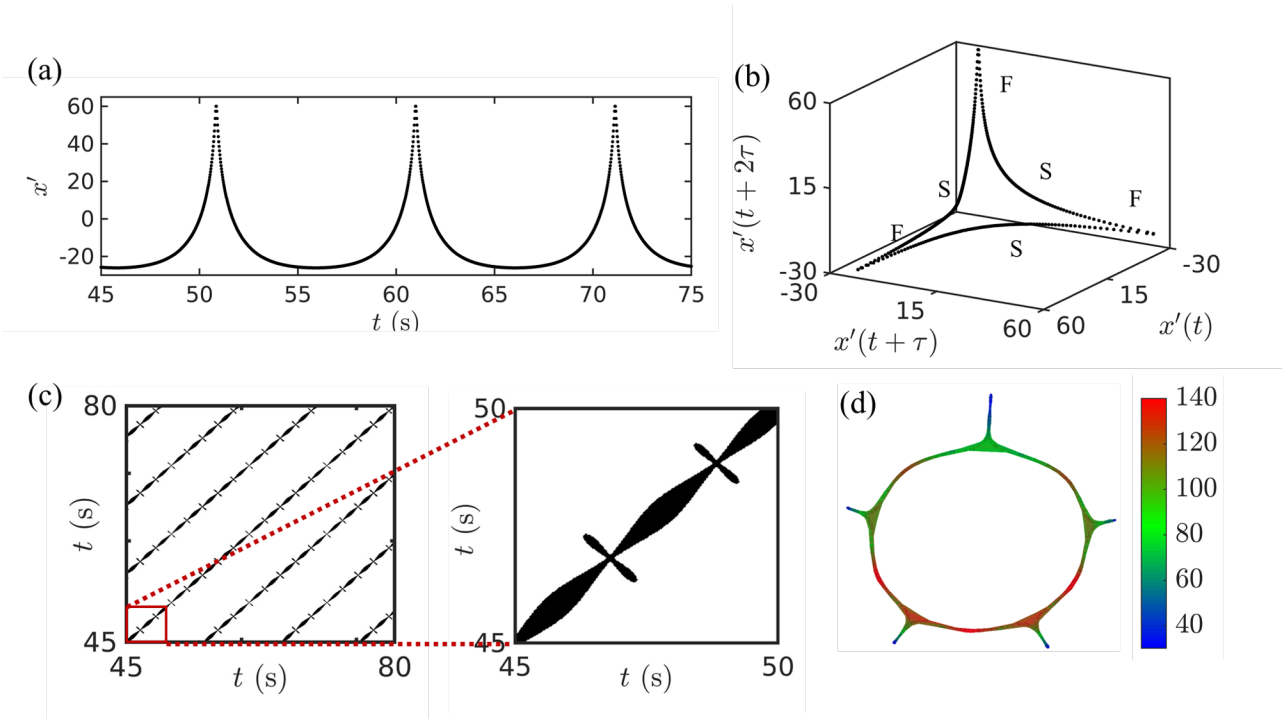

FIG. 4. (a) A synthetic periodic spiky signal is constructed after modifying the output of Izhikevich's neuron spiking model. The values used in the model are a = 0.1, b = 0.2, c = -60, d = 8, and I = 110. ((b)-(d) The reconstructed phase space, RP along with its zoomed view portion, and RN, respectively, for signal shown in (a). The parameters fixed for plotting (b)-(d) are τ = 102, d = 10, and RR = 0.05. The color code in plotting RN is based on degree of nodes.

is predominantly slow with many nodes having very high number of connections (red and green color). The fast regions in the phase space are present in the protrusions comprising nodes with low degree (blue). In contrast to the RN of Van der Pol system, we observe that only nodes with high and medium degree (red and green colour, respectively) occupy the ring structure. However, the protrusions on the ring structure in the RN are crowded by the nodes with low degree (blue colour). This characteristic behavior must arise out of some fundamental difference in these two slow-fast systems, which is being reflected on their respective recurrence properties. Also, we identify that the micro-patterns in the RP and the RN are different from the ones obtained for the Van der Pol system.

We also analyze the recurrence properties of the well-known Hodgkin-Huxley model which exhibits slow-fast oscillations[81,125]. The Hodgkin-Huxley model is represented by the follow-

ing equations described below.

$$\begin{aligned} \dot{V} &= \tfrac{1}{C_m}\left[I - g_{Na}m^3h(V-E_{Na}) - g_K n^4(V-E_K) - g_L(V-E_L)\right] \\ \dot{m} &= \alpha_m(V)(1-m) - \beta_m(V)m \\ \dot{n} &= \alpha_n(V)(1-n) - \beta_n(V)n \\ \dot{h} &= \alpha_h(V)(1-h) - \beta_h(V)h. \end{aligned} \tag{17}$$

Here, v is the the potential, I is current per unit area, and g_i is the maximum value of conductance where i corresponds to either one of potassium (K), sodium (Na) or leak channel (L). Variables: m, n, and h are non-dimensional quantities with values between 0 to 1 and are associated with the potassium channel activation, sodium channel activation, and sodium channel inactivation, respectively. In Eq. 17, the constant parameters used are: E_{Na} = 115 mV; E_K = -12 mV; E_L = 10.6 mV; g_{Na} = 120 mS/cm^2; g_K = 36 mS/cm^2; g_L = 0.3 mS/cm^2; C_m = 1 μF/cm^2. The corresponding steady state values for the gating variables, α and β, are related to the potential V, as described in the support equations (Eq. 18). The set of equations are solved using Euler's method.

$$\begin{aligned} \alpha_h &= 0.07\exp\left[\tfrac{-(V+65)}{20}\right], \quad \beta_h = \tfrac{1}{1+\exp\left[\frac{-(V+35)}{10}\right]}, \\ \alpha_m &= 0.1\tfrac{V+40}{1-\exp\left[\frac{-(V+40)}{10}\right]}, \quad \beta_m = 4\exp\left[\tfrac{-(V+65)}{18}\right], \\ \alpha_n &= 0.01\tfrac{V+55}{1-\exp\left[\frac{-(V+55)}{10}\right]}, \quad \beta_n = 0.125\exp\left[\tfrac{-(V+65)}{80}\right]. \end{aligned} \tag{18}$$

In Fig. 5a, we plot the time series of the membrane potential, V, obtained for I = 10 in Eq. 17. We observe that V exhibits limit cycle behavior with slow-fast timescales. In the corresponding three-dimensional phase portrait in Fig. 5b, we observe that certain regions are slow (marked S) while other regions are fast (marked F). The corresponding RP also exhibits unique micro-structures on top of the diagonal lines (see Fig. 5c). The sword-like structure occurs for similar reasons as the perpendicular lines observed in the RP of the synthetic spiky signal in Fig. 4c. The corresponding RN in Fig. 5d exhibits a protrusion made up of high degree nodes, and several clusters built of medium degree nodes on top of a ring of low degree nodes. Thus, the RN of the Hodgkin-Huxley model discussed contain both the features seen in Fig. 3b,d and Fig. 4d.

After analyzing the phase space dynamics and recurrence properties of these three synthetic periodic slow-fast signals along with a sine wave, we understood that slow-fast systems exhibit characteristic features on top of the closed loop structure in the RN. Moreover, the

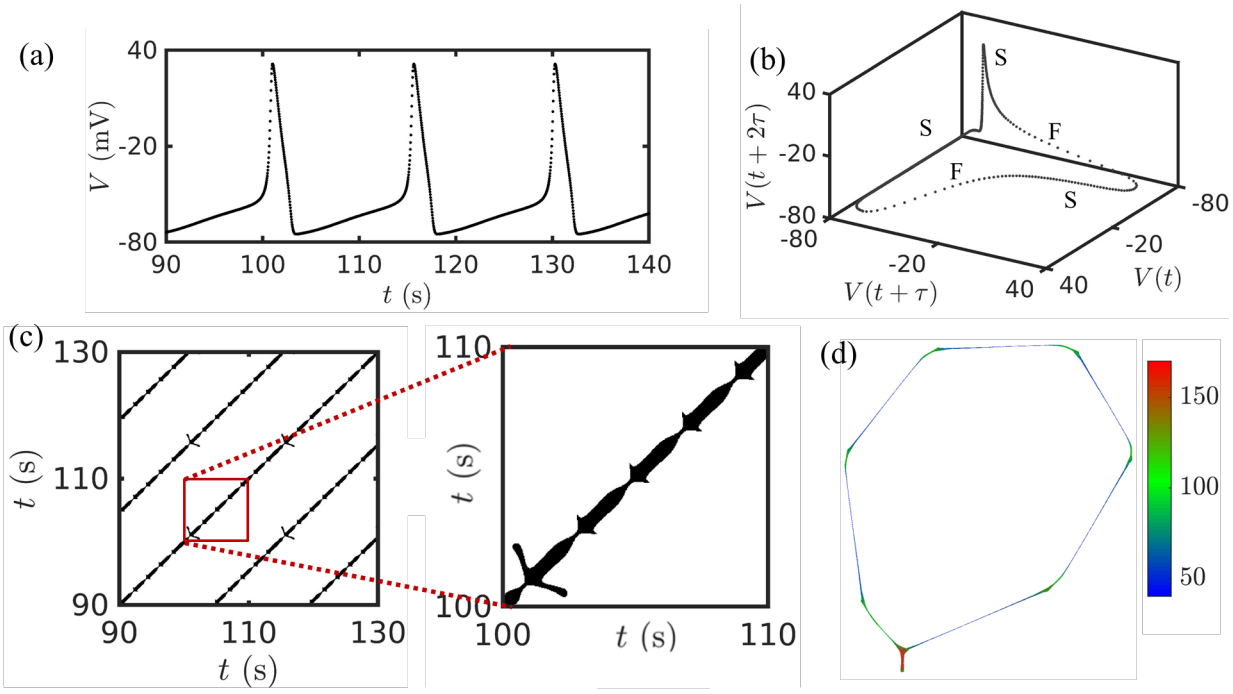

FIG. 5. (a) Time series of membrane potential (V) obtained from Hodgkin-Huxley model for I=10. (b)-(d) The reconstructed phase space, RP along with its zoomed view portion, and RN, respectively, for signal shown in (a). The parameter fixed for plotting (b)-(d) are $d = 7$, $\tau = 66$, and RR $= 0.05$. The color code in plotting RN is based on degree of nodes.

RP of such systems is manifested by unique micro-patterns pertaining to slow-fast dynamics over the diagonal lines.

B. Recurrence analysis of high-dimensional experimental systems

In order to confirm the aforementioned observations in the slow-fast dynamics of real-world data, we present the results of the investigation of two different time series acquired from experiments in a laboratory scale gas turbine-type turbulent combustor and a model liquid rocket combustor during the state of an oscillatory instability, known as thermoacoustic instability[44]. Here, thermoacoustic instability is a dynamical state featured by large amplitude, self-sustained periodic oscillations in the acoustic pressure, $p'(t)$, and heat release rate, $\dot{q}'(t)$, of the system. The occurrence of such phenomenon overwhelms the thermal protection systems, compromises the control and structural stability of gas turbine and rocket engines[19,44].

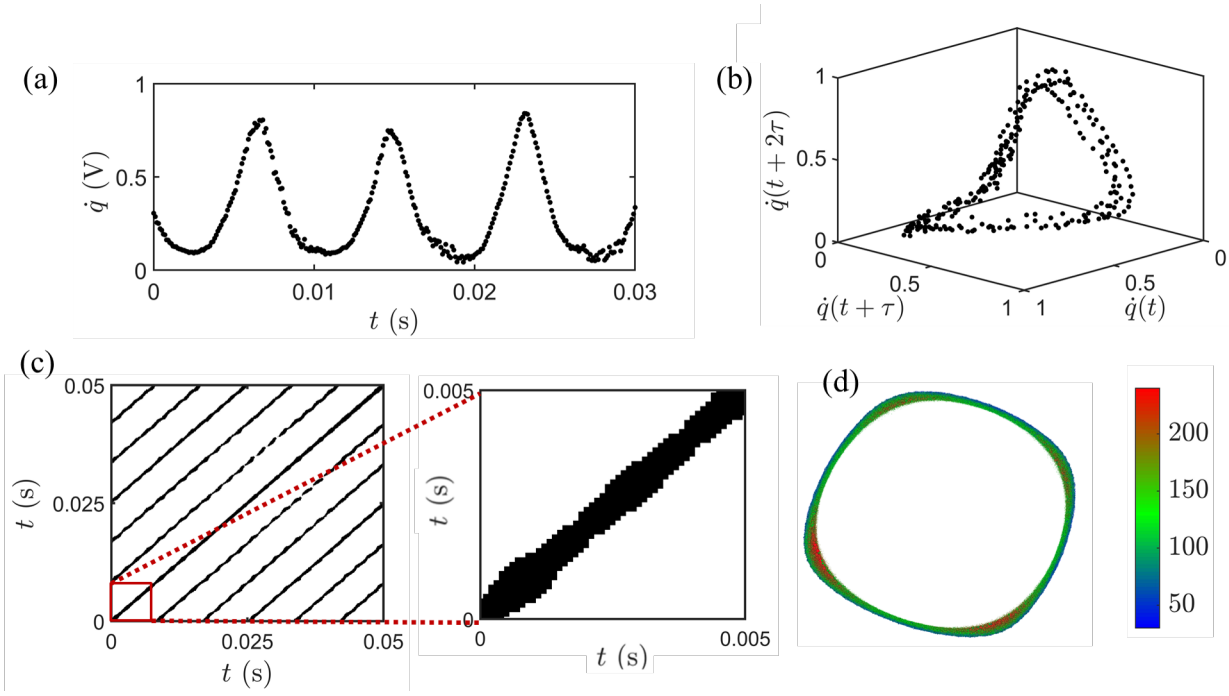

FIG. 6. (a) Time series of heat release rate fluctuations ($\dot{q}$') during thermoacoustic instability acquired from a laboratory scale turbulent combustor. (b)-(d) The reconstructed phase space, RP along with its zoomed view portion, and RN, respectively, plotted for the signal shown in (a). The parameter fixed for plotting (b)-(d) are $d = 12$, $tau = 20$, and RR = 0.1.

First, in Fig. 6a,b, we consider the time series of heat release rate fluctuations ($\dot{q}(t)$) and the corresponding reconstructed phase space obtained during the state of thermoacoustic instability for the gas turbine type turbulent combustor. We observe that the time series is spiky[104], exhibiting a clear departure from sinusoidal signals. The spikiness in the signal (see Fig. 6a) is attributed to the instantaneous heat release as a result of the impingement of the large scale coherent vortex structure carrying fuel-air mixture against the walls of the combustor[127].

In the corresponding phase space of the heat release rate signal in Fig. 6b, we observe a distorted closed loop structure, indicative of the non-uniform evolution of consecutive state points due to the presence of slow and fast timescales. However, such slow and fast timescales are not too separated when compared to the earlier phase space of synthetic signals. In the RP of this signal (see Fig. 6c), we see the presence of continuous diagonal lines, indicating sustained periodicity in the oscillations. The corrugations along the diagonal lines arise due to the presence of the slow and fast timescales in the phase space. The RN for this signal

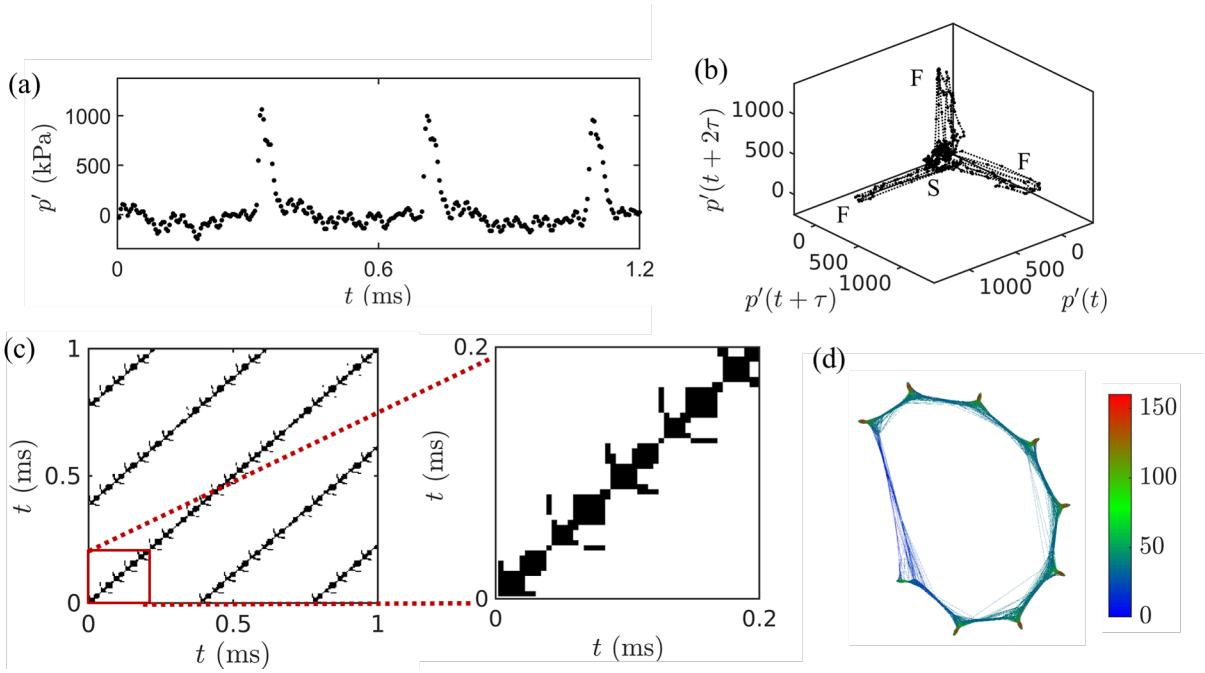

FIG. 7. (a) Time series of acoustic pressure fluctuations ((p') during thermoacoustic instability acquired from a multi-element model liquid rocket combustor. (b)-(d) The reconstructed phase space, RP along with its zoomed view portion, and RN, respectively, for the signal shown in (a). The parameter fixed for plotting (b)-(d) are $d = 10$, $\tau = 21$, and RR $= 0.05$.

(see Fig. 6d) looks similar to that of Van der Pol as there are clusters of high degree nodes (red colour) on the ring of medium degree (green colour) nodes. The clusters pertain to the slow regions in the phase space.

Finally, we investigate the time series of acoustic pressure oscillations ($p'(t)$) in a multi-element model liquid rocket combustor during the state of thermoacoustic instability[41] (see Fig. 7a). We observe that a major portion of the cycle is spent in the slow relaxation phase with a momentary jump in the pressure due to the fast compression phase of the signal. Physically, due to an increase in the speed of sound during the compression phase, the compression side catches up with the expansion side of the pressure wave. This phenomena known as wave steepening results in an abrupt increase in the amplitude of the pressure oscillation[23]. Under favorable conditions, the steepened wave manifests as a shock wave in the flow-field. Such wave steepened shock waves are commonly observed in the pressure oscillations of a rocket combustor.

The reconstructed phase space of this pressure signal, shown in Fig. 7b, is similar to the

phase portrait shown in Figs. 4b & 5b, wherein the trajectory moves along the three axes to complete one oscillation cycle. Unlike the usual closed loop structure of the phase space trajectory of periodic signals observe in the previous slow-fast systems, the phase space of pressure signal exhibits a peculiar shape. We attribute this geometrical difference of the phase space attractor to the vast divergence in the slow and fast timescales in the rocket system.

The RP and the RN for the pressure oscillations are plotted in Fig. 7c,d, respectively. The RP of the pressure signal contains a unique micro-structure arising due to the presence of slow-fast timescales. On top of the diagonal line indicating periodicity of the signal, we observe thick regions divided by a thin region. The thick regions emerge due to the increased trapping of the phase space trajectory in slow timescale while the thin regions correspond to the fast timescale. The RN of this signal looks similar to Fig. 4d based on its topological similarity. The protrusions in the RN in Fig. 7d are made up of high degree (red) nodes, unlike the RN in Fig. 4d where the protrusions are made up of low degree (blue) nodes.

With the understanding gained from analyzing the various synthetic and experimental systems in this study, we noticed that the dynamics of slow-fast systems can be understood based on their recurrence properties. From the RNs, we observed that some slow-fast systems exhibit protrusions, while other systems display clustering. Each slow-fast system imparts a signature micro-structure over the diagonal lines in their corresponding RP. It is also interesting to note that even though both the real-world systems (discussed in this study) operate in the state of thermoacoustic instability, both the systems exhibit different RN topology due to a difference in their underlying mechanisms that generate such oscillations.

C. Recurrence network measures

Next, we exclusively study the transition from stable operation to thermoacoustic instability in the chamber acoustic pressure oscillations of the model liquid rocket combustor using network measures. In Fig. 8, we show the time series displaying the transition from stable operation to thermoacoustic instability via intermittency. We partition the time series into 100 segments, each of size of around 16 cycles of the dominant frequency (2650 Hz). A recurrence network is constructed for each of these slices. Then, we obtain the corresponding adjacency matrices.

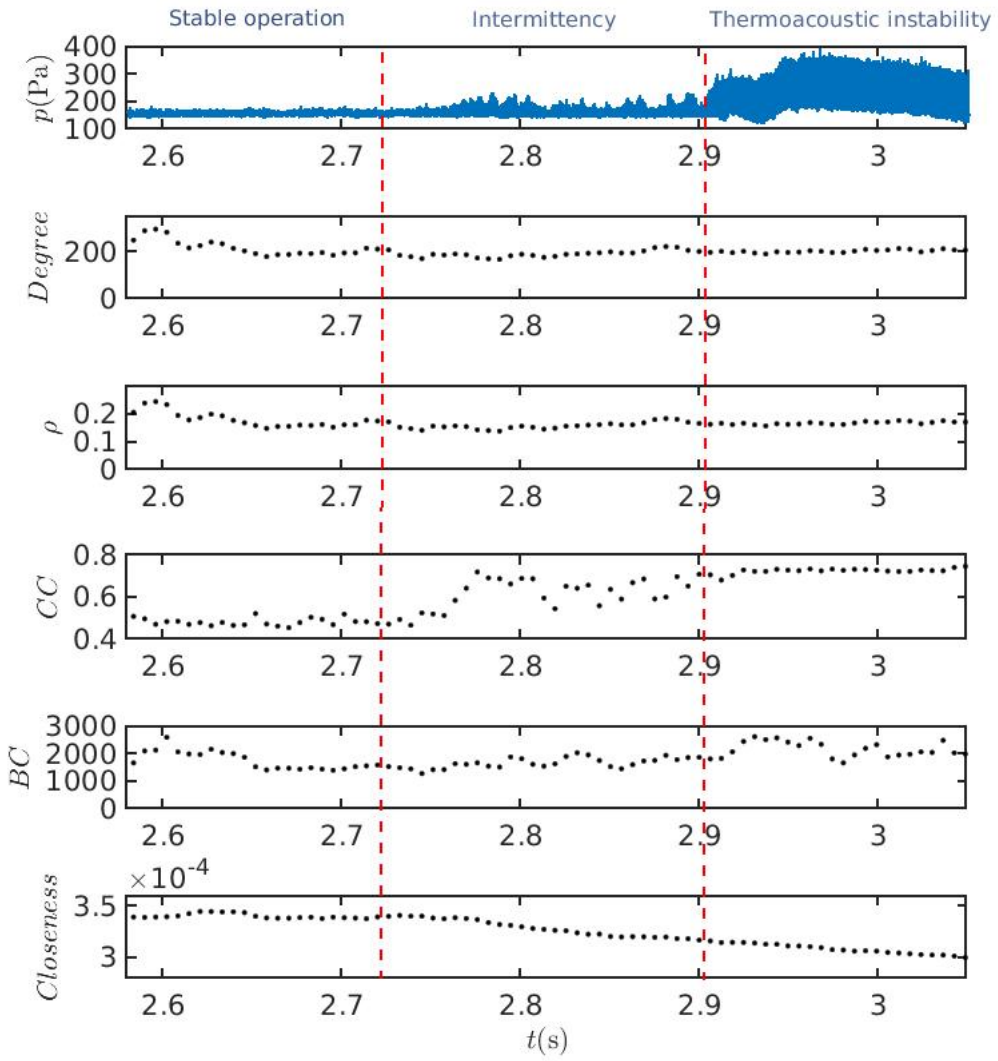

FIG. 8. The time series of the model liquid rocket combustor exhibiting the transition from stable operation to thermoacoustic instability via intermittency. The variation of network measures (b) Degree, (c) Link density, (d) Mean clustering coefficient, (e) Mean betweenness centrality, and (f) Mean closeness centrality are plotted. The parameter fixed for plotting (b)-(f) are $d = 10$, $\tau = 21$, and RR $= 0.05$. A window size of around 16 cycles of the dominant frequency (2650 Hz) is used.

Then, we calculate the network measures: average degree ($Degree$), mean link density (ρ), mean clustering coefficient (CC), mean betweenness centrality (BC), and mean closeness centrality ($Closeness$). We observe that there is a discernible trend in the variation of mean clustering coefficient (CC). The value of CC increases from around 0.4 during

stable operation to 0.8 during thermoacoustic instability with intermediate values during intermittency. For the other measures, we do not observe any distinguishable trend. For *Closeness*, we detect the decreasing trend. However, the variation in the measure is very low.

IV. SUMMARY

In this study, for the first time, the recurrence properties of slow-fast systems are studied with the aid of recurrence plots and recurrence networks. A systematic approach is adopted by first performing the analysis on low-dimensional synthetic signals before understanding high-dimensional experimental time series. We discovered that slow-fast systems exhibit different recurrence properties compared to periodic systems which operate on a single timescale. We observe that unique features about the slow-fast system can be obtained from the micro-patterns along the diagonal line in the RPs, unlike straight lines for harmonic signals. Further, we identify characteristic features on the corresponding RN topologies for slow-fast systems. In addition to the closed ring structure, we observe protrusions and clustering in the RN. We believe that this study will have wide ranging applications to understand the dynamics of various diverse systems across natural sciences, medicine, econometrics and engineering.

CHAPTER 4
PREPARATION OF TOOLS FOR SPATIO-TEMPORAL ANALYSIS

Network theory is one of the more popular way to investigate spatiotemporal analysis of complex systems such as brain, climate, epidemics and turbulent flows. We enlist three major types of network construction to investigate the spatiotemporal dynamics during the transition to thermoacoustic instability from a state of stable combustor operation.

I. SPATIAL NETWORK ANALYSIS

In this methodology, we construct spatial correlation networks from velocity and heat release field. For example, let us examine the construction of spatial correlation networks from the heat release field. We consider the pixels in the high-speed chemiluminescence images as nodes of the network. Any pair of nodes (i and j) are connected if the Pearsons correlation coefficient (R_{ij}) between the time series of heat release rate at the two nodes are above a threshold (say R_{ij}=0.5). Next, we examine the network properties such as degree, local clustering coefficient, betweenness centrality and closeness centrality. These network measures help us to identify the critical regions in the flow field that control the spatiotemporal dynamics during a particular state of combustor operation. A very high value of degree and local clustering coefficient for a region implies that the heat release rate fluctuations at the nodes in the region are highly correlated amongst themselves. Such a region could be responsible for the coherent heat release occurring during thermoacoustic instability.

As an example, we constructed an unweighted spatial correlation network constructed from the heat release rate oscillations for intermittency and thermoacoustic instability. We use the CH* chemiluminescence images acquired at a rate of 100 kHz for this analysis. The imaging is performed on the optically accessible window located at the edge of the rectangular combustor. We plot the network measures for both intermittency and thermoacoustic instability in Fig. 1. We observe a distinct spatial feature which is preserved in all the network measures considered.

In Fig. 1, the *degree* quantifies the amount of interaction each spatial location has with

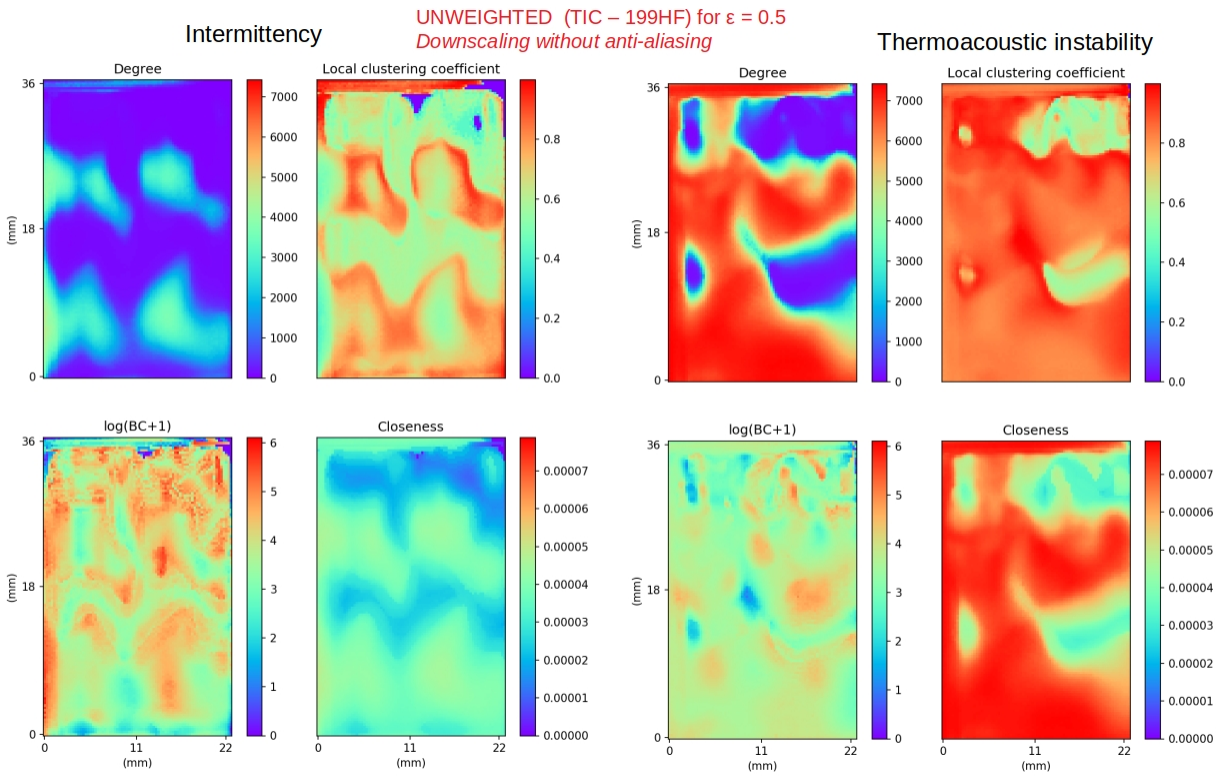

FIG. 1. Spatial variation of the network measures: degree, local clustering coefficient, betweenness centrality and closeness centrality, in the spatial network of heat release rate oscillations during the dynamical states of intermittency (left) and thermoacoustic instability (right) in the model multi-element liquid rocket combustor. The The networks are unweighted (i.e. links are binarized) and constructed individually for the dynamical states of intermittency and thermoacoustic instability using a linear correlation coefficient of 0.5. The networks are built from the high-speed CH* chemiluminescence images acquired at rate of 100 kHz at the optically accessible window located at the edge of the rectangular combustor.

the all the other spatial nodes in the networks. We observe that *degree* increases significantly in a number of spatial locations during the onset of thermoacoustic instability. This signifies that the number of interactions are enhanced during the state of thermoacoustic instability as compared to intermittency. The measure *local clustering coefficient* quantifies the extent to which two neighbors of a given spatial node are connected to each other. As observed during the state of thermoacoustic instability, we obtain high values in the *local clustering coefficient*, promoting the formation of clusters of acoustic power production in the combustor. The measure *betweenness centrality* highlights the most critical spatial nodes

in the number through which the cluster of nodes can be spanned. The measure *closeness* quantitatively estimates the proximity of a spatial location to all other nodes in the network. Higher values of *closeness* of a node translates to a spatial location more suited for quick information transfer from the selected node to all other nodes in the network. During thermoacoustic instability, we observe high values of *closeness* signifies the well connected close group of nodes in the network. Such patterns and interactions in the spatiotemporal domain can be characterized by the framework of complex networks.

We could construct weighted spatial correlation networks instead of unweighted ones. In weighted network analysis, we assign a 'weight' to the link between the nodes. For our study, the weight could be Pearsons correlation coefficients. Unlike the unweighted network analysis, weighted network analysis gives the strength of the interaction between the nodes. However, this advantage comes with a cost. Weighted network analysis is much more difficult and computationally very costly.

II. TIME VARYING SPATIAL NETWORK ANALYSIS

The real world complex systems inherently evolve over time. Time-varying network analysis accounts for this dynamical nature of connectivity[128]. Time-varying spatial network analysis is used extensively in the area of brain research to analyze the dynamical functional connectivity of the brain network[129,130]. Recently, Krishnan et al.[131] used time-varying local acoustic power networks to investigate the emergence of large clusters of acoustic power sources at the onset of thermoaocuticinstability in a turbulent bluff body stabilized combustor. A similar approach can be adopted in the current study to investigate the spatiotemporal evolution of acoustic power sources during the transition to thermoaocustic instability. To this end, we need to perform simultaneous acoustic pressure measurements and high-speed chemiluminescence imaging during the trnasition to thermoaocustic instability. As discussed above, we consider each pixel of high-speed flame image as a node of the network. As we have a transverse mode thermoacoustic instability in our model rocket engine, we can consider the domiant transverse acoustic mode for the pressure variation across the width of the combustor. With this information, we can multiply at each instant of time, the heat release rate at each pixel ($\dot{q}\prime$) with the corresponding acoustic pressure ($p\prime$). For constructing the local acoustic power networks[131], we consider only those nodes where $p\prime\dot{q}\prime > 0$. While

establishing the link between the nodes, we consider only the nearest neighbours of a node. Thus, we shall be able to examine the spatiotemporal evolution of clusters of acoustic power sources during the transition to thermoaocustic instability.

We can consturct time varying turbulence network from the vorticity field obtained from either (1) CFD simulation or (2) experimental data. Using the appraoch followed by Taira et al.[132], we shall investigate the topology of the networks during the transition to thermoaocustic instability in the model rocket combustor. The presence of hubs in the network will pave for devising efficient control strategies. However, time-varying network analyisis is computationally very time-consuming. We need to incorporate parallel computing and need to run the codes in high-performance workstations to obtain the results on time.

III. MULTILAYER NETWORK ANALYSIS

We know that the dynamics of a liquid rocket combustor is influenced by the hydrodynamic flow-field, acoustics and heat release rate field sustained by combustion reactions. All these subsystems interact in a complex manner to generate thermoacoustic instability. Hence, a complex network approach studying only the dynamics of either heat release rate field or the velocity field in isolation would not unearth the spatiotemporal coupled behavior. Hence, we need to adopt the framework of multilayer networks wherein, a layered approach of network construction is adopted. Each layer can represent a subsystem with links running both within each layer (captures interactions within subsystem) and across layer (captures interactions across subsystems). Such a network framework would allow us to characterize the conditions and identify the spatiotemporal coupling behaviors.

Further, the multilayer network framework can be modified to study spatial networks (time averaged) as well as spatiotemporal networks (space as well as time varies). For the liquid rocket combustor, we shall construct spatial correlation networks from heat release field and velocity field and investigate the spatiotemporal coupling between these two fields during the different stages of combutor operation using various network measures. Such an approach is unprecedented in thermoacoustics literature.

CHAPTER 5
CONCLUSIONS

The dynamics of acoustics pressure oscillations during the transition from stable operation to thermoacoustic instability in a model multi-element rocket combustor is analyzed. The combustor was operated under a preheated high pressure turbulent flow rig in a fuel rich condition, to better simulate the operational conditions in a real rocket engine (or motor). We observe that the transition from small amplitude stable operation to large amplitude thermoacoustic instability occurs through intermittency. The waveform during thermoacoustic instability is highly nonlinear, consisting of typically steepened pressure wavefronts leading to the formation of shock waves, and is significantly different from the sinusoidal limit cycle oscillations typically seen in gas turbine combustors. Further, we detect the dynamical switching between period-3 and period-4 oscillations in an apparently random manner during thermoacoustic instability and the periodic epochs of intermittency. Such complex limit cycle dynamics are seldom seen in gas turbine combustors.

To demonstrate the efficacy of measures based on dynamical systems and complex system theory, we present a recurrence based measure ($RATIO$) and two fractal based measures (multifractal spectrum width and the Hurst exponent), that can be used to distinguish different states of combustor operation. We found that these measures are more robust than the existing measures such as root mean square of the oscillations, amplitude, maximum of cross correlation *etc.* in distinguishing the dynamical state of a rocket engine.

Subsequently, using the method of recurrence analysis, we established that the chamber acoustic pressure oscillations during thermoacoustic instability in the model liquid rocket combustor behaves like a slow-fast system. The unique features of the oscillations are captured in the recurrence plot and the recurrence network. We also established the presence of such features in the oscillations of heat release rate in a model gas turbine type turbulent combustor and several well-known models such as Van der Pol system, a modified form of Izhikevich's neuron spiking model and Hodgkin-Huxley model.

Through this work, we have successfully translated modern tools from nonlinear time series analysis to understand the complex oscillations arising in liquid rocket engines. In the process, we showed that the signals in a rocket combustor can be better understood and modelled utilizing such an approach. The measures illustrated in this study can be used to

validate the CFD multi-fidelity simulations used for optimizing the stability and performance metrics of the rocket combustor. Such an approach can reduce the developmental timescales of a rocket engine and also aid engineers in testing the rockets subjected to design and operational envelope modifications.

CHAPTER 6
FUTURE WORK

I. SYNCHRONIZATION

Synchronization theory has been used recently in understanding the phenomenon of the onset of thermoacoustic instability (Pawar et al.[104];Guan et al.[133]; Mondal et al.[55,56] and also providing several active control strategies for the mitigation of such instability (Thomas et al.[134,135]; Mondal et al.[136]). This theory primarily deals with the understanding of the instantaneous coupling between two or more oscillators. Pawar et al.[104] showed that the onset of thermoacoustic instability is a synchronization phenomenon of the acoustic field and unsteady heat release rate field in the combustor. Moreover, synchronization of oscillators leads to an emergence of spatiotemporal order in the reaction field during the state of thermoacoustic instability from a disordered state observed during stable operation of the combustor[55]. The application of synchronization theory to data from liquid rocket combustor at different operating conditions would help in gaining the insights in temporal coupling of acoustic and turbulent reaction fields of the combustor. Simultaneous analysis of flames from multiple injectors with the acoustic field would improve understanding of the phenomenon of the onset of thermoacoustic instability in such liquid rocket combustor. A phenomenological model based on the array of coupled Stuart Landau oscillators or a network of Rossler oscillators coupled with Van der Pol oscillator can be developed. Such a type of modeling would help in understanding the emergent behaviour of the spatial field of the liquid rocket combustor and also infer the dominant coupling mechanisms existing in the system.

II. COMPLEX NETWORK

Complex systems approach is a new approach to the science of studying how the interaction among the constituent parts gives rise to the collective behavior of a system[137]. This science is providing a new perspective on the understanding of the physical, biological, ecological and social universe. One of the popular tools to study such complex systems is complex networks[138]. In complex network approach, the components of a complex system are considered as nodes and the interactions between the nodes are represented as links. Complex networks have emerged as one of the most efficient tools in the analysis of di-

verse fields such as brain, epidemics, climate modelling, sociology, economics, physiology, computer science and transport engineering[138].

A turbulent flow induces a large number of degrees of freedom to the thermoacoustic system. The thermoacoustic system in a turbulent combustor involves the interplay of a number of processes such as molecular mixing, turbulent transport, chemical kinetics and acoustic waves operating over a range of length and time scales. The complex interaction of these processes over such large number of degrees of freedom gives rise to a rich spatiotemporal dynamics with the emergence of order at the onset of thermoacoustic instability[139]. This prompts us to consider the thermoacoustic system in a turbulent liquid rocket combustor as a complex system.

Most of the real world complex systems have nodes and edges embedded in space. Transportation networks, internet, social and contact networks, power grids and neural networks are all examples where space is relevant and just studying the network topology without taking into consideration the spatial information of the nodes gives incomplete and sometimes misleading results[140]. Characterizing and understanding the structure and dynamics of spatial networks is thus vital in obtaining deeper insights in the study of complex systems.

Spatial network analysis is also used in the study of fluid mechanical systems. In climatology, researchers explored the statistical interdependence between the time series of an observable, such as precipitation, at two different locations (spatially embedded nodes) to construct spatial networks[141,142]. Scarsoglio, Iacobello and Ridolfi[143] identified coherent structures in the flow field using correlation network based on the time series of the kinetic energy of a three dimensional forced isotropic turbulent flow field obtained from direct numerical simulation. Recently, Unni *et al.*[144] performed spatial network analysis, in a model gas turbine type turbulent combustor with bluff body stabilized flame, based on the correlation between the time series of local velocity obtained from particle image velocimetry (PIV). The authors identified the *critical* regions in the flow field using network centrality measures for each dynamical state. They hypothesized that the *critical* region is the optimal location for implementing passive control strategies.

As a future study, we can employ spatial correlation network analysis to investigate flame dynamics from the high-speed chemiluminescence imaging. The network centrality measures calculated from the correlation networks would enable us to identify the *critical* region during the transition to thermoacoustic instability.

Recently, Taira, Nair and Brunton[132] characterized a two dimensional decaying isotropic turbulent flow field, obtained from direct numerical simulation, based on the vortical interaction between the fluid elements at different grid points. They constructed time-varying spatial networks from the velocity field. They discovered that the vorticity interaction is characterized by an inverse power-law. As a future study, we can investigate the velocity field, obtained either from (1) CFD simulation or (2) experiments, during the transition to thermoacoustic instability by constructing time-varying spatial networks using Biot-Savart law. This study would shed light into the structure of the vorticity interaction during the different dynamical regimes of rocket engine operation.

So far, researchers have examined the local acoustic power ($p\prime\dot{q}\prime$) field and the velocity field separately during the different states of the combustor operation. Multilayer network analysis[145] is one promising approach that can provide insight into the interaction of these two fields as the combustor dynamics transitions from the state of combustion noise to thermoacoustic instability via intermittency.

These studies, however, are computationally very intensive and hence time-consuming. Also, there exists no universal framework to construct relevant complex networks. As a result, the complex network construction has to be driven by the problem we are trying to solve. Once the complex networks are constructed, suitable measures have to be formulated which can help us unravel previously unknown phenomena and shed light on the critical locations in the system.

III. BASIN STABILITY FUNCTION

One of the major problems faced by the rocket industry is to discriminate between the data-sets which exhibit transition to thermoacoustic instability and those data-sets which stay within stable amplitude levels, for the same set of control parameters. Measures based on basin stability function backed approaches[146] could potentially accomplish this task. Given that the framework of basin stability functions is in its infancy, it would take a significant amount of time and insight to achieve this task. Also, the data requirements for such an approach involves stringent constraints such as data length, high resolution, sampling *etc.*. To the best knowledge of the authors', there exists no proper framework where basin stability function has been used on experimental results at the time of this writing. As a

result, a significant amount of time needs to be invested, working with collaborators who have championed this methodology. Therefore, a thorough literature survey on the topic to adopt a relevant framework is necessary prior to application of this approach to classify time series of chamber acoustic pressure oscillations in liquid rockets.

RESEARCH OUTPUT

I. JOURNAL PAPERS

(1) Kasthuri, P., Pavithran, I., Pawar, S.A., Sujith, R.I., Gejji, R., and Anderson, W., 2019. Dynamical transitions in a liquid rocket combustor. Chaos: An Interdisciplinary Journal of Nonlinear Science (Under review).

(2) Kasthuri, P., Pavithran, I., Krishnan, A., Pawar, S.A., Sujith, R.I., Gejji, R., and Anderson, W., Marwan, N., Kurths, J., 2019. Recurrence properties of slow-fast systems. Chaos: An Interdisciplinary Journal of Nonlinear Science (Under preparation).

II. CONFERENCE

(1) Pavithran, I., Kasthuri, P., Krishnan, A., Pawar, S.A., Sujith, R.I., Gejji, R., and Anderson, W., Marwan, N., Kurths, J., 2019. Eighth International Symposium on Recurrence Plots, August 21-23, 2019,Zhenjiang, China.

REFERENCES

[1]D. T. Harrje, "Liquid propellant rocket combustion instability," Tech. Rep. (NASA SP-194, 1972).

[2]V. Young, *Liquid rocket engine combustion instability*, Vol. 169 (AIAA, 1995).

[3]J. W. S. Rayleigh, Nature **18**, 319 (1878).

[4]R. Levine, in *Symposium (International) on Combustion*, Vol. 10 (Elsevier, 1965) pp. 1083–1099.

[5]R. H. Sabersky, Journal of Jet Propulsion **24**, 172 (1954).

[6]L. Crocco, in *Symposium (International) on Combustion*, Vol. 10 (Elsevier, 1965) pp. 1101–1128.

[7]S. Rubin, Journal of Spacecraft and Rockets **3**, 1188 (1966).

[8]B. T. Zinn, AIAA Journal **11**, 1492 (1973).

[9]F. Blomshield, J. Crump, H. Mathes, R. A. Stalnaker, and M. Beckstead, Journal of Propulsion and Power **13**, 349 (1997).

[10]L. Crocco and S. I. Cheng, "Theory of combustion instability in liquid propellant rocket motors," Tech. Rep. (Princeton University, 1956).

[11]W. A. Sirignano, Combustion Science and Technology **187**, 162 (2015).

[12]L. Crocco, D. Harrje, and F. Reardon, AIAA Journal **2**, 1631 (1964).

[13]B. Zinn, AIAA journal **6**, 1966 (1968).

[14]L. Crocco, Journal of the American Rocket Society **21**, 163 (1951).

[15]L. Crocco, Journal of the American Rocket Society **22**, 7 (1952).

[16]B. T. Zinn and E. A. Powell, in *Symposium (International) on Combustion*, Vol. 13 (Elsevier, 1971) pp. 491–503.

[17]C. Mitchell, L. Crocco, and W. Sirignano, Combustion Science and Technology **1**, 35 (1969).

[18]F. Blomshield, in *43rd AIAA/ASME/SAE/ASEE Joint Propulsion Conference & Exhibit* (2007) p. 5803.

[19]T. C. Lieuwen, *Unsteady combustor physics* (Cambridge University Press, 2012).

[20]F. Culick and P. Kuentzmann, "Unsteady motions in combustion chambers for propulsion systems," Tech. Rep. (NATO Research and Technology Organization Neuilly-Sur-Seine (France), 2006).

[21]Y. Fabignon, J. Dupays, G. Avalon, F. Vuillot, N. Lupoglazoff, G. Casalis, and M. Prévost, Aerospace science and technology **7**, 191 (2003).

[22]J. Messineo, J.-Y. Lestrade, J. Hijlkema, and J. Anthoine, Journal of Propulsion and Power **32**, 1386 (2016).

[23]M. Tyagi and R. I. Sujith, Journal of Fluid Mechanics **492**, 1 (2003).

[24]A. Hirschberg, J. Gilbert, R. Msallam, and A. Wijnands, The Journal of the Acoustical Society of America **99**, 1754 (1996).

[25]G. A. Flandro, S. R. Fischbach, and J. Majdalani, Physics of Fluids **19**, 094101 (2007).

[26]M. Tyagi and R. Sujith, in *9th AIAA/CEAS Aeroacoustics Conference and Exhibit* (2003) p. 3146.

[27]E. Price, Fundamentals of Solid-Propellant Combustion **90**, 733 (1984).

[28]S. Gröning, J. S. Hardi, D. Suslov, and M. Oschwald, Journal of Propulsion and Power , 560 (2016).

[29]T. Shimada, M. Hanzawa, T. Morita, T. Kato, T. Yoshikawa, and Y. Wada, AIAA journal **46**, 947 (2008).

[30]P. P. Popov and W. A. Sirignano, Journal of Propulsion and Power **32**, 620 (2016).

[31]A. Urbano, L. Selle, G. Staffelbach, B. Cuenot, T. Schmitt, S. Ducruix, and S. Candel, Combustion and Flame **169**, 129 (2016).

[32]R. Hart and F. McClure, The journal of chemical physics **30**, 1501 (1959).

[33]R. Hart, J. Bird, R. Cantrell, and F. McClure, AIAA Journal **2**, 1270 (1964).

[34]F. E. Culick, Astronautica Acta **12**, 113 (1966).

[35]F. Culick, Combustion Science and Technology **2**, 179 (1970).

[36]G. Bloxsidge, A. Dowling, and P. Langhorne, Journal of fluid mechanics **193**, 445 (1988).

[37]T. Selvakumaran and N. Kadiresh, Propellants, Explosives, Pyrotechnics (2017).

[38]Y. Guan, P. Liu, B. Jin, V. Gupta, and L. K. Li, Experimental Thermal and Fluid Science (2018).

[39]L. Crocco, ARS Journal **30**, 159 (1960).

[40]R. Lecourt and R. Foucaud, in *23rd Joint Propulsion Conference* (1987) p. 1772.

[41]M. R. Orth, C. Vodney, T. Liu, W. Z. Hallum, T. L. Pourpoint, and W. E. Anderson, in *2018 AIAA Aerospace Sciences Meeting* (2018) p. 1185.

[42]L. Kabiraj, R. I. Sujith, and P. Wahi, Journal of Engineering for Gas Turbines and Power **134**, 031502 (2012).

[43]S. A. Pawar and R. I. Sujith, Journal of the Combustion Society of Japan **60**, 99 (2018).

[44]M. P. Juniper and R. I. Sujith, Annual Review of Fluid Mechanics **50**, 661 (2018).

[45]V. Nair and R. I. Sujith, Journal of Fluid Mechanics **747**, 635 (2014).

[46]V. Nair, G. Thampi, and R. I. Sujith, Journal of Fluid Mechanics **756**, 470 (2014).

[47]V. R. Unni and R. I. Sujith, in *52nd AIAA/SAE/ASEE Joint Propulsion Conference* (2016) p. 4649.

[48]H. Gotoda, Y. Shinoda, M. Kobayashi, Y. Okuno, and S. Tachibana, Physical Review E **89**, 022910 (2014).

[49]S. Domen, H. Gotoda, T. Kuriyama, Y. Okuno, and S. Tachibana, Proceedings of the Combustion Institute **35**, 3245 (2015).

[50]V. Nair, G. Thampi, S. Karuppusamy, S. Gopalan, and R. I. Sujith, International journal of spray and combustion dynamics **5**, 273 (2013).

[51]M. Murugesan and R. I. Sujith, Journal of Propulsion and Power **32**, 707 (2016).

[52]V. Godavarthi, V. R. Unni, E. Gopalakrishnan, and R. I. Sujith, Chaos: An Interdisciplinary Journal of Nonlinear Science **27**, 063113 (2017).

[53]V. Godavarthi, S. A. Pawar, V. R. Unni, R. I. Sujith, N. Marwan, and J. Kurths, Chaos: An Interdisciplinary Journal of Nonlinear Science **28**, 113111 (2018).

[54]S. A. Pawar, R. Vishnu, M. Vadivukkarasan, M. Panchagnula, and R. I. Sujith, Journal of Engineering for Gas Turbines and Power **138**, 041505 (2016).

[55]S. Mondal, V. R. Unni, and R. I. Sujith, Journal of Fluid Mechanics **811**, 659 (2017).

[56]S. Mondal, S. Pawar, and R. I. Sujith, Chaos: An Interdisciplinary Journal of Nonlinear Science **27**, 103119 (2017).

[57]F. Takens, in *Dynamical systems and turbulence, Warwick 1980* (Springer, 1981) pp. 366–381.

[58]A. M. Fraser and H. L. Swinney, Physical review A **33**, 1134 (1986).

[59]A. H. Nayfeh and B. Balachandran, *Applied nonlinear dynamics: analytical, computational, and experimental methods* (John Wiley & Sons, 2008).

[60]L. Cao, Physica D: Nonlinear Phenomena **110**, 43 (1997).

[61]J. Eckmann, S. O. Kamphorst, D. Ruelle, *et al.*, World Scientific Series on Nonlinear Science Series A **16**, 441 (1995).

[62]N. Marwan, *Encounters with neighbours: current developments of concepts based on recurrence plots and their applications* (Norbert Marwan, 2003).

[63]C. L. Webber Jr and N. Marwan, Theory and Best Practices (2015).

[64]C. Webber Jr and J. Zbilut, in *Soc. Neurosci. Abstr*, Vol. 21 (1995) p. 1402.

[65]J. Feder, *Fractals* (Springer Science & Business Media, 2013).

[66]B. Mandelbrot, science **156**, 636 (1967).

[67]B. B. Mandelbrot, *The fractal geometry of nature*, Vol. 173 (WH freeman New York, 1983).

[68]J. W. Kantelhardt, S. A. Zschiegner, E. Koscielny-Bunde, S. Havlin, A. Bunde, and H. E. Stanley, Physica A: Statistical Mechanics and its Applications **316**, 87 (2002).

[69]E. A. F. E. Ihlen, Frontiers in physiology **3**, 141 (2012).

[70]B. Kerres, A. Cronhjort, and M. Mihaescu, in *The 12th International Conference on Turbochargers and Turbocharging, London, UK, 17-18 May, 2016* (2016).

[71]R. K. Zia, E. F. Redish, and S. R. McKay, American Journal of Physics **77**, 614 (2009).

[72]D. Grech and Z. Mazur, Physical Review E **87**, 052809 (2013).

[73]V. Suyal, A. Prasad, and H. P. Singh, Solar Physics **260**, 441 (2009).

[74]H. A. Abderrahmane, F. Paquet, and H. D. Ng, Combustion Theory and Modelling **15**, 205 (2011).

[75]R. C. Hilborn *et al.*, *Chaos and nonlinear dynamics: an introduction for scientists and engineers* (Oxford University Press on Demand, 2000).

[76]J. Hołyst, M. Żebrowska, and K. Urbanowicz, The European Physical Journal B-Condensed Matter and Complex Systems **20**, 531 (2001).

[77]N. Marwan, M. C. Romano, M. Thiel, and J. Kurths, Physics reports **438**, 237 (2007).

[78]M. Nurujjaman, R. Narayanan, and A. S. Iyengar, Physics of Plasmas **16**, 102307 (2009).

[79]S. A. Pawar and R. I. Sujith, in *Droplets and Sprays* (Springer, 2018) pp. 403–430.

[80]L. Glass, Nature **410**, 277 (2001).

[81]E. M. Izhikevich, *Dynamical systems in neuroscience* (MIT press, 2007).

[82]A. M. Zhabotinsky, Chaos: An Interdisciplinary Journal of Nonlinear Science **1**, 379 (1991).

[83]A. C. Lazer and P. McKenna, Siam Review **32**, 537 (1990).

[84]T. C. Lieuwen and V. Yang, *Combustion instabilities in gas turbine engines: operational experience, fundamental mechanisms, and modeling* (American Institute of Aeronautics and Astronautics, 2005).

[85]R. Bertram and J. E. Rubin, Mathematical biosciences **287**, 105 (2017).

[86]H. Kantz and T. Schreiber, IEE Proceedings-Science, Measurement and Technology **145**, 279 (1998).

[87]F. Lordon, Journal of Evolutionary Economics **7**, 1 (1997).

[88]J. Leeman, D. Saffer, M. Scuderi, and C. Marone, Nature communications **7**, 11104 (2016).

[89]P. Johnson and A. Sutin, The Journal of the Acoustical Society of America **117**, 124 (2005).

[90]T. Vallaitis, C. Koos, R. Bonk, W. Freude, M. Laemmlin, C. Meuer, D. Bimberg, and J. Leuthold, Optics express **16**, 170 (2008).

[91]E. W. Bruun, P. Ambus, H. Egsgaard, and H. Hauggaard-Nielsen, Soil Biology and Biochemistry **46**, 73 (2012).

[92]S.-T. Chen, Y.-J. Guo, H.-N. Huang, W.-M. Kung, K.-K. Tseng, and S.-Y. Tu, Journal of medical systems **38**, 54 (2014).

[93]S. Dutta, Journal of Statistical Mechanics: Theory and Experiment **2010**, P12021 (2010).

[94]J. Millman, *Integrated electronics* (Tata McGraw Hill, 2010).

[95]R. T. Schumacher, S. Garoff, and J. Woodhouse, The Journal of Adhesion **81**, 723 (2005).

[96]M. Desroches, J. Guckenheimer, B. Krauskopf, C. Kuehn, H. M. Osinga, and M. Wechselberger, Siam Review **54**, 211 (2012).

[97]C. Kuehn, *Multiple time scale dynamics*, Vol. 191 (Springer, 2015).

[98]B. Van der Pol, The London, Edinburgh, and Dublin Philosophical Magazine and Journal of Science **2**, 978 (1926).

[99]R. FitzHugh, Biophysical journal **1**, 445 (1961).

[100]D. Wang and D. Terman, IEEE transactions on neural networks **6**, 283 (1995).

[101]S. H. Strogatz, *Nonlinear dynamics and chaos: with applications to physics, biology, chemistry, and engineering* (CRC Press, 2018).

[102]C. Kuehn, Physica D: Nonlinear Phenomena **240**, 1020 (2011).

[103]N. Berglund and B. Gentz, *Noise-induced phenomena in slow-fast dynamical systems: a sample-paths approach* (Springer Science & Business Media, 2006).

[104]S. A. Pawar, A. Seshadri, V. R. Unni, and R. I. Sujith, Journal of Fluid Mechanics **827**, 664 (2017).

[105]N. Marwan, N. Wessel, U. Meyerfeldt, A. Schirdewan, and J. Kurths, Physical review E **66**, 026702 (2002).

[106]N. Marwan, The European Physical Journal Special Topics **164**, 3 (2008).

[107]A. Facchini, H. Kantz, and E. Tiezzi, Physical Review E **72**, 021915 (2005).

[108]F. Censi, V. Barbaro, P. Bartolini, G. Calcagnini, A. Michelucci, G. Gensini, and S. Cerutti, Annals of biomedical engineering **28**, 61 (2000).

[109]A. Fabretti and M. Ausloos, International Journal of Modern Physics C **16**, 671 (2005).

[110]M. Stöckl, D. Plück, and M. Lames, Mathematical and Computer Modelling of Dynamical Systems **23**, 399 (2017).

[111]L. Kabiraj and R. Sujith, Journal of Fluid Mechanics **713**, 376 (2012).

[112]V. Nair and R. Sujith, International Journal of Aeroacoustics **15**, 312 (2016).

[113]V. Nair and R. I. Sujith, Combustion Science and Technology **187**, 1821 (2015).

[114]N. Marwan, M. Thiel, and N. R. Nowaczyk, arXiv preprint physics/0201062 (2002).

[115]A. J. Corrado, *Dynamics of complex systems* (CRC Press, 2019).

[116]R. V. Donner, Y. Zou, J. F. Donges, N. Marwan, and J. Kurths, New Journal of Physics **12**, 033025 (2010).

[117]R. V. Donner, M. Small, J. F. Donges, N. Marwan, Y. Zou, R. Xiang, and J. Kurths, International Journal of Bifurcation and Chaos **21**, 1019 (2011).

[118]Z.-K. Gao, X.-W. Zhang, N.-D. Jin, R. V. Donner, N. Marwan, and J. Kurths, EPL (Europhysics Letters) **103**, 50004 (2013).

[119]H. Gotoda, H. Kinugawa, R. Tsujimoto, S. Domen, and Y. Okuno, Physical Review Applied **7**, 044027 (2017).

[120]G. M. Ramírez Ávila, A. Gapelyuk, N. Marwan, T. Walther, H. Stepan, J. Kurths, and N. Wessel, Philosophical Transactions of the Royal Society A: Mathematical, Physical and Engineering Sciences **371**, 20110623 (2013).

[121]S. V. George, R. Misra, and G. Ambika, arXiv preprint arXiv:1907.10602 (2019).

[122]A.-L. Barabási *et al.*, *Network science* (Cambridge university press, 2016).

[123]M. Bastian, S. Heymann, and M. Jacomy, in *Third international AAAI conference on weblogs and social media* (2009).

[124]E. M. Izhikevich, IEEE Transactions on neural networks **14**, 1569 (2003).

[125]M. Díaz, A. Jose, O. Téquita, and F. Naranjo, Ingeniería y Ciencia **12**, 93 (2016).

[126]N. Marwan, J. F. Donges, Y. Zou, R. V. Donner, and J. Kurths, Physics Letters A **373**, 4246 (2009).

[127]A. Seshadri, V. Nair, and R. Sujith, Combustion Theory and Modelling **20**, 441 (2016).

[128]P. Holme and J. Saramäki, Physics reports **519**, 97 (2012).

[129]M. Valencia, J. Martinerie, S. Dupont, and M. Chavez, Physical Review E **77**, 050905 (2008).

[130]K. W. Doron, D. S. Bassett, and M. S. Gazzaniga, Proceedings of the National Academy of Sciences **109**, 18661 (2012).

[131]A. Krishnan, R. Sujith, N. Marwan, and J. Kurths, Journal of Fluid Mechanics **874**, 455 (2019).

[132]K. Taira, A. G. Nair, and S. L. Brunton, Journal of Fluid Mechanics **795** (2016).

[133]Y. Guan, L. K. Li, B. Ahn, and K. T. Kim, Chaos: An Interdisciplinary Journal of Nonlinear Science **29**, 053124 (2019).

[134]N. Thomas, S. Mondal, S. A. Pawar, and R. Sujith, Chaos: An Interdisciplinary Journal of Nonlinear Science **28**, 033119 (2018).

[135]N. Thomas, S. Mondal, S. A. Pawar, and R. Sujith, Chaos: An Interdisciplinary Journal of Nonlinear Science **28**, 093116 (2018).

[136]S. Mondal, S. A. Pawar, and R. Sujith, Journal of Fluid Mechanics **864**, 73 (2019).

[137]Y. Bar-Yam, S. R. McKay, and W. Christian, Computers in Physics **12**, 335 (1998).

[138]A.-L. Barabási, Nature Physics **8**, 14 (2011).

[139]N. B. George, V. R. Unni, M. Raghunathan, and R. Sujith, Journal of Fluid Mechanics **849**, 615 (2018).

[140]M. Barthélemy, *Spatial networks* (Springer, 2018).

[141]A. A. Tsonis and P. J. Roebber, Physica A: Statistical Mechanics and its Applications **333**, 497 (2004).

[142]N. Malik, B. Bookhagen, N. Marwan, and J. Kurths, Climate dynamics **39**, 971 (2012).

[143]S. Scarsoglio, G. Iacobello, and L. Ridolfi, International Journal of Bifurcation and Chaos **26**, 1650223 (2016).

[144]V. R. Unni, A. Krishnan, R. Manikandan, N. B. George, R. Sujith, N. Marwan, and J. Kurths, Chaos: An Interdisciplinary Journal of Nonlinear Science **28**, 063125 (2018).

[145]S. Boccaletti, G. Bianconi, R. Criado, C. I. Del Genio, J. Gómez-Gardenes, M. Romance, I. Sendina-Nadal, Z. Wang, and M. Zanin, Physics Reports **544**, 1 (2014).

[146]P. J. Menck, J. Heitzig, N. Marwan, and J. Kurths, Nature physics **9**, 89 (2013).